Quantum Wavepacket Ab Initio Molecular Dynamics for Extended Systems

Xiaohu Li[†] and Srinivasan S. Iyengar[*]

Department of Chemistry and Department of Physics, Indiana University, 800 East Kirkwood Avenue, Bloomington, IN 47405

ABSTRACT: In this paper, we introduce a symmetry-adapted quantum nuclear propagation technique that utilizes distributed approximating functionals for quantum wavepacket dynamics in extended condensed-phase systems. The approach is developed with a goal for implementation in quantum—classical methods such as the recently developed quantum wavepacket ab intio molecular dynamics (QWAIMD) to facilitate the study of extended systems. The method has been numerically benchmarked for extended electronic systems as well as protonic conducting systems that benefit from quantum nuclear treatment. Vibrational properties are computed for the case of the protonic systems through use of a novel velocity—flux correlation function. The treatment is found to be numerically accurate and efficient.
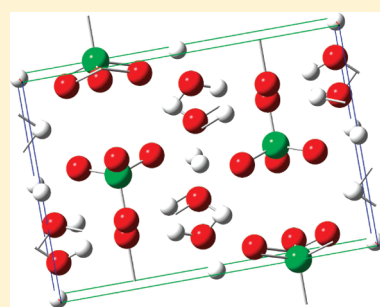
1. INTRODUCTION

Recently,[1−11] we introduced a methodology that accurately computes quantum dynamical effects in a subsystem while simultaneously treating the motion of the surrounding atoms and coupled changes in electronic structure. The approach is quantum—classical[12−23] and involves the synergy between a time-dependent quantum wavepacket description and ab initio molecular dynamics. As a result, the approach is called quantum-wavepacket ab initio molecular dynamics (QWAIMD). Because quantum dynamics is performed on a grid, the predominant bottleneck is the computation of the grid-based, time-dependent electronic structure potential and gradients generated by the motion of the classical nuclei.[1−4] This limitation is partially surmounted through the following methodological improvements. (a) A time-dependent deterministic sampling (TDDS) technique was introduced in refs 3, 4, and 9, which when combined with numerical methods such as an efficient wavelet compression scheme and low-pass-filtered Lagrange interpolation,[4] provides computational gains of many orders of magnitude (Figure 1). (b) Multiple diabatic reduced single-particle electronic density matrices are propagated simultaneously with the quantum wavepacket in ref 6, and the associated diabatic states are used to construct an adiabatic surface at every instance in time using a nonorthogonal CI formalism. The diabatic approximation allows reuse of the two-electron integrals during the on-the-fly potential energy surface computation stage and leads to substantial reduction in computational costs (Figure 1). QM/MM and QM/QM generalizations to QWAIMD have also been completed.[5] We have utilized QWAIMD to compute vibrational properties of hydrogen-bonded clusters inclusive of quantum nuclear effects[4] and have also adopted the method to study hydrogen tunneling in enzyme-active sites.[7,24] The quantum dynamics scheme in QWAIMD has also been used to develop a technique known as multistage ab initio wavepacket dynamics (MSAIWD) to treat open, nonequilibrium electronic systems.[10,11]

Here, we generalize QWAIMD to compute quantum dynamical effects in extended systems. This generalization is geared toward the following set of problems: (a) Extended, solid-state, hydrogen-bonded networks that involve short, strong hydrogen bonds have recently been studied[25−37] to provide protonic and superprotonic conductors[25,26,38] that may be stable alternatives to fuel cells. These materials also allow para-electric to ferroelectric or antiferroelectric transitions, and in many cases, the physical properties of these materials change dramatically upon H/D isotope substitution. Inelastic neutron scattering studies[26,27,34] and solid-state NMR[31,32] methods have been utilized to probe the structural and vibrational properties in such extended hydrogen-bonding networks. Protonic and superprotonic conduction[25,26,38] is thought to arise from coupled dynamics of multiple protons in such extended system. In a similar vein, imidazole chains[39,40] have been considered as alternatives to proton wires present in nafion.[39−42] Imidazole chains are similar to water wires in terms of their propensity to display conductivity properties comparable to the Grottuss mechanism for proton transfer.[36,43,44] (b) Miniature lithium batteries have recently been studied for improved energy storage.[45−48] It has been shown that lithium ions in such confined environments can display quantum nuclear behavior,[49] and the methodologies provided in this publication will be used in the future to study the confined quantum nuclear effect from a lattice of lithium ions bound by solid polymer electrolytes.[45,46] (c) Extended electronic systems such as those found in self-assembled monolayers are also included.[10,11] The electronic dynamics that includes the extended nature of the system may be critical in computing the nonequilibrium electronic flux and conductance through such systems. To treat such problems, here, we generalize QWAIMD to compute quantum dynamical effects arising in extended (periodic) systems.

ACS Publications © XXXX American Chemical Society

A

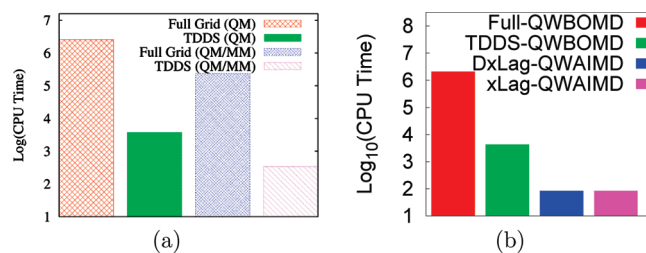dx.doi.org/10.1021/jp112389m | *J. Phys. Chem. A* XXXX, XXX, 000–000

Figure 1. (a) Computational expense for QWAIMD with and without time-dependent deterministic sampling (TDDS). Note that in all cases, the vertical axis is the logarithm of CPU time. TDDS provides enormous reduction in computational time. Compare the two histgrams on the left in (a) to note the ~3.5 orders of magnitude reduction in computational effort afforded by TDDS. Similarly, the two histograms on the right in (a) indicate that TDDS continues to reduce computational effort when combined with QM/MM calculation of the potential surface. (b) Further reduction in computation time is facilitated through the introduction of a propagation scheme that involves multiple diabatic states.[6] Note the two right histogram plots in (b).

The paper is organized as follows. In section 2, an introduction to the methodological aspects of QWAIMD is provided, where we also outline the quantum dynamical propagation. QWAIMD is a quantum—classical separation method. Hence, numerical benchmarks from previous publications that lay out the foundations of applicability of QWAIMD are discussed in Appendix A. The system chosen in Appendix A is a highly anharmonic hydrogen-bonded cluster, and the results are compared with other methods as well as with experiment. In section 3, we introduce generalizations to the quantum propagation scheme utilized in QWAIMD, where the propagation is adapted to the inherent symmetry of the potential. For example, for the periodic protonic conductor systems,[25−28,34] a quantum propagator that accounts for the inherent periodicity of the problem (inclusive of k-point symmetry) is desirable, and section 3 aims to provide such an approach. Because the quantum propagation scheme utilized here is based on the "distributed approximating functional" propagation formalism, the expressions derived in section 3 are called the extended symmetrized distributed approximating functional propagator (ESDAF-P). Section IIIA describes the appropriate symmetry-adapted nuclear coordinates that follow the dynamics presented in section IIIB. The numerical benchmarks are organized as follows. In section IVA, the free-particle case is considered. In section IVB, an illustration is provided where a free-particle system is perturbed by a weak potential. This example is pertinent to the uniform electron gas treatment and also the nearly free particle system such as a lattice of confined lithium ions,[45−48] where again analytical solutions are available from perturbation theory. The analytical solutions are provided in Appendix B. This helps benchmark the accuracy and computational effectiveness of the ESDAF-P formalism. In section IVC, we provide a preliminary demonstration of the use of ESDAF-P in the quantum dynamics of protons in extended protonic conductor systems.

2. BRIEF DESCRIPTION OF QUANTUM WAVEPACKET AB INITIO MOLECULAR DYNAMICS (QWAIMD)

We first outline QWAIMD, before discussing generalizations to the quantum dynamics scheme that will facilitate the treatment of extended systems. As noted in the Introduction, results that provide a benchmark for the quantum—classical separation in QWAIMD are outlined in Appendix A. Comparison with experiment and other theoretical methods is also presented in Appendix A.

The main features of QWAIMD are as follows. The quantum dynamical evolution is described through a third-order Trotter factorization of the quantum propagator.[1,50−52] For local potentials, the potential energy operator is diagonal in the coordinate representation. The free propagator, $\exp\{-iKt/\hbar\}$ may be approximated

in a number of ways. One approach is to recognize that this operator is diagonal in the momentum representation. Hence, fast Fourier transforms may be employed[51,53−57] to obtain the result of the free propagator operating on a wavepacket. Other alternatives include (a) the use of direct[58] or iterative Lanczos[59] based diagonalization of the full Hamiltonian and the subsequent representation of the evolution operator $\exp\{-iHt/\hbar\}$ using the eigenstates, (b) the use of Chebychev polynomial approximations for the propagator[58,60−65] that are based on the Jacobi—Anger formula,[66] (c) the use of eigenstates of components of the Hamiltonian operator,[67] and (d) the use of Feynman path integration techniques.[68−75] The list here is not exhaustive and a detailed discussion on the topic may be found in refs 76 and 77. In all cases, the Hamiltonian needs to be approximated in some representation. Two representations that are popular in quantum dynamics are the discrete variable representations (DVR)[78−80] and the distributed approximating functionals (DAF).[81−86] The implementation of QWAIMD discussed in refs 1−11 employs the free propagator approximated in the coordinate representation using a formally exact distributed approximation functional (DAF)[1,2,81,87,88] expression

$$\left\langle R_{QM} \left| \exp\left\{-\frac{iK\Delta t}{\hbar}\right\} \right| R'_{QM} \right\rangle_{DAF} \equiv \tilde{K}(R_{QM} - R'_{QM}, M_{DAF}, \sigma, \Delta t)$$

$$= \frac{1}{\sigma(0)} \sum_{n=0}^{M_{DAF}/2} \left(\frac{\sigma(0)}{\sigma(\Delta t)}\right)^{2n+1} \left(\frac{-1}{4}\right)^n \frac{1}{n!} (2\pi)^{-1/2}$$

$$\exp\left\{-\frac{(R_{QM} - R'_{QM})^2}{2\sigma(\Delta t)^2}\right\} H_{2n}\left(\frac{R_{QM} - R'_{QM}}{\sqrt{2}\sigma(\Delta t)}\right) \quad (1)$$

Here, $\{\sigma(\Delta t)\}^2 = \sigma(0)^2 + i\Delta t\hbar/M_{QM}$, $\{H_{2n}(x)\}$ are even order Hermite polynomials (note that the arguments for the Hermite polynomials and the Gaussian function, $[(R_{QM} - R'_{QM})/(2^{1/2}\sigma(\Delta t))]$, are complex in general), and R_{QM} represents the quantum mechanical degrees of freedom. The free propagation of a wavepacket is then given in the discrete coordinate representation as

$$\chi(R^i_{QM}, \Delta t) = \Delta x \sum_j \langle R^i_{QM} | \exp\{-iK\Delta t/\hbar\} | R^j_{QM} \rangle \chi(x_j, 0)$$

$$= \Delta x \sum_j \tilde{K}(R^i_{QM} - R^j_{QM}, M_{DAF}, \sigma, \Delta t)\chi(R^j_{QM}, 0)$$

$$(2)$$

The parameters M_{DAF} and σ above together[1,81] determine the accuracy and efficiency of the DAF propagator. As M_{DAF} increases, the accuracy as well as the computational expense increases. It is

B

dx.doi.org/10.1021/jp112389m |J. Phys. Chem. A XXXX, XXX, 000–000

worth noting a few characteristics of eq 1. For any fixed level of approximation, determined by the choice of parameters M_{DAF} and $\sigma'(0)$, the kernel in eq 1 only depends on the quantity $(R_{QM}^i - R_{QM}^j)$, which is the distance between points in the coordinate representation and goes to 0 as this quantity becomes numerically large on account of the Gaussian dependence. This yields a banded, Toeplitz matrix approximation to eq 1 for any finite M_{DAF} and $\sigma'(0)$. [The (i,j)th element of a Toeplitz matrix depends only on $|i - j|$.] On account of these properties, eq 1 provides great simplicity in computation of the quantum propagation. In fact, as shown in ref 11, it is possible to computationally implement this propagation scheme in a form that includes a series of scalar–vector operations with the total number of operations given by

$$N + \sum_{i=1}^{W-1} 2(N - i) = N(2W - 1) - W(W - 1) \approx \mathcal{O}(N) \tag{3}$$

where W is the width of the propagator in the coordinate representation, that is, the maximum value of $(R_{QM}^i - R_{QM}^j)/\Delta x$ in eq 2 such that all values of the free propagator are less than a numerical threshold for $(R_{QM}^i - R_{QM}^j)/\Delta x > W$. The quantity N is the number of grid points used in the discretization scheme. Because W does not depend on N [W in fact depends on M_{DAF} and $\sigma'(0)$, that is, the required accuracy of propagation], this scaling goes as $\mathcal{O}(N)$ for large grids. Thus, the approach allows for efficient quantum dynamical treatment. In all calculations performed here, $M_{DAF} = 20$ (that is, all even Hermite polynomials up to order 20 are used), and $\sigma/\Delta = 1.5744$, where Δ is the grid spacing.

The utilization of the DAF is, however, not critical to QWAIMD, and other propagation schemes such as those highlighted at the beginning of this section can be readily employed. The choice here, and in the previous QWAIMD studies, is governed by the demonstrated accuracy of the DAF,[89−95] where it has been benchmarked[89,90] and found to compare favorably with other propagation methods (see Table 1 in refs 89 and 90 for benchmarks and the Appendix in ref 11 for computational scaling).

For the remaining portion of this section, two different implementations of QWAIMD are described in sections IIA and IIB.

A. Time-Dependent Deterministic Sampling (TDDS)-Based Implementation of QWAIMD. In one form of QWAIMD,[3,4] the evolution of the classical nuclei involves the wavepacket averaged Hellmann−Feynman forces obtained from electronic structure calculations carried out on the discrete wavepacket grid.

$$\mathbf{R}_C(t + \Delta t) = \mathbf{R}_C(t) + \dot{\mathbf{R}}_C(t)\Delta t - \frac{\Delta t^2}{2}\mathbf{M}^{-1/2}\mathscr{F}_{\mathbf{R}_C}(t)\mathbf{M}^{-1/2} \tag{4}$$

$$\dot{\mathbf{R}}_C(t + \Delta t) = \dot{\mathbf{R}}_C(t) - \frac{\Delta t}{2}\mathbf{M}^{-1/2}[\mathscr{F}_{\mathbf{R}_C}(t) + \mathscr{F}_{\mathbf{R}_C}(t + \Delta t)]\mathbf{M}^{-1}/2 \tag{5}$$

$$\mathscr{F}_{\mathbf{R}_C}(t) = \left\langle \chi(t) \left| \frac{\partial E(\{\mathbf{R}_C, \mathbf{P}_C\}, R_{QM})}{\partial \mathbf{R}_C}(t) \right|_{\mathbf{P}_C} \right| \chi(t) \right\rangle \tag{6}$$

where the time dependence is explicitly noted and the symbol $\{|\mathbf{P}_C\}$ is said to imply that the gradients are to be computed either under the usual variational conditions on the electronic density matrix or by maintaining them as constant.[96,97] To minimize the number of electronic structure calculations carried out on the grid while

directing their placement for maximal efficiency, an adaptive TDDS procedure has been introduced and benchmarked in refs 3, 4, and 9. This technique allows large-scale reductions (by many orders of magnitude) in computation time, with little loss in accuracy.[3,4] The mathematical form of the original TDDS function described in refs 3 and 4 is a function of the quantum nuclear degrees of freedon, R_{QM}, as follows. The TDDS function is chosen to be directly proportional to the wavepacket probability density, $\rho(R_{QM})$, and gradient of the potential, $V'(R_{QM})$, while being inversely proportional to the potential, $V(R_{QM})$. That is

$$\omega_0(R_{QM}) \propto \frac{[\tilde{\rho}(R_{QM}) + 1/I_\chi] \times [\tilde{V}'(R_{QM}) + 1/I_{V'}]}{\tilde{V}(R_{QM}) + 1/I_V} \tag{7}$$

where $\tilde{\rho}$, $\tilde{V}'$, and $\tilde{E}$ are shifted and normalized[3,4] according to

$$\tilde{V}(R_{QM}) \propto \frac{V(R_{QM}) - V_{min}}{V_{max} - V_{min}} \tag{8}$$

and similarly for $\tilde{\rho}(R_{QM})$ and $\tilde{V}'(R_{QM})$. The quantities V_{max} and V_{min} are the maximum and minimum values for the potential, respectively. The overall sampling function, $\omega_0(R_{QM})$, is L^1-normalized according to

$$\|\omega_0(R_{QM})\|_1 = \int |\omega_0(R_{QM})| \, dR_{QM} = 1 \tag{9}$$

Large values of the TDDS function represent areas where sampling should occur. The construction of TDDS has physical justifications that ensure that both classical and quantum (tunneling) regions of the dynamics are equally sampled.[3,4,9] As shown in ref 3, the choice of parameters, $I_\chi = 1$, $I_{V'} = 3$, and $I_V = 1$, retains significant distribution in both the classically allowed (minimum energy regions) and classically forbidden (classical turning point) regions of the potential and leads to a large reduction in computational cost, with little perceivable loss in accuracy. [As a result of the definition of $\tilde{\rho}(R_{QM})$, $\tilde{V}(R_{QM})$, and $\tilde{V}'(R_{QM})$ according to eq 8, these are dimensionless, and hence, the parameters I_χ, $I_{V'}$, and I_V are also dimensionless.] In addition to eq 7, other forms of the TDDS functions that employ Shannon's entropy function[98−101] have also been derived and benchmarked in ref 9.

The TDDS function is evaluated at every instant in time to determine the grid points where the potential and gradients will be evaluated for the next time step. For this purpose, the TDDS function is written as a linear combination of Haar wavelets[4]

$$\omega(x) \propto \frac{[\tilde{\rho} + 1/I_\chi] \times \left[\tilde{E}' + 1/I_{E'}\right]}{\tilde{E} + 1/I_E}$$

$$= \sum_{i=0}^{N_{GEN}} \underbrace{\sum_{j_1=0}^{a^i-1} \cdots \sum_{j_{N_{Dim}}=0}^{a^i-1}}_{} c_{i,\{j\}} \left\{ \prod_{k=1}^{N_{Dim}} \mathcal{H}\left(a^i x^k - \frac{j_k N_Q}{a^i}\right) \right\} \tag{10}$$

where the Haar scaling function, $\mathcal{H}(x)$ is a square function equal to 1 for $0 \leq x \leq 1$ and 0 otherwise. The quantity N_{GEN} is the number of wavelet generations, and the underbrace below the summations is meant to indicate that there are N_{Dim} summations, $[j_1, j_2, ..., j_{N_{Dim}}]$, and $c_{i,\{j\}}$ implies that the coefficients depend on i and the entire set of j-indices. The Haar wavelets, $\{\mathcal{H}(a^i x - j_k N_Q/a^i)\}$ comprise a hierarchy of translated and dilated forms of $\mathcal{H}(x)$. Only the Haar scaling function is used because the Haar wavelet function is the orthogonal complement of the Haar scaling function and is not positive semidefinite, which is one of the requirements on ω. The

C

dx.doi.org/10.1021/jp112389m |*J. Phys. Chem. A* XXXX, XXX, 000–000

quantity x^k, in eq 10, is the kth component of the N_{Dim} dimensional vector, and a is chosen to be 2 or 3, that is, we employ two- and three-scale functions in our scheme.

Once the subset of grid points for on-the-fly potential energy determination is computed using the TDDS function, the value of the potential at the remaining points is obtained through Hermite curve interpolation.[102] The forces on classical atoms are subsequently determined through a low-pass-filtered Lagrange interpolation technique introduced in ref 4. Time-dependent deterministic sampling has played a pivotal role in converting QWAIMD into an efficient computational tool through reduction of computational costs by about three to four orders of magnitude.[4] (See Figure 1.)

B. Further Computational Enhancements through Diabatic Extensions to QWAIMD. To further enhance the computational scaling of QWAIMD, in ref 6, we introduced a diabatic generalization to QWAIMD. Multiple single-particle electronic density matrices were simultaneously propagated through an extended Lagrangian scheme. Following this, the Slater determinant wave functions corresponding to the density matrices were used in a nonorthogonal CI formalism, on-the-fly, to obtain the instantaneous adiabatic states. Computational efficiency arises through the diabatic approximation for the multiple density matrices; this essentially necessitates a limited dependence of the quantum nuclear degrees of freedom on the individual electronic density matrix states. Once this condition is enforced, it is found that two-electron integrals can be reused over the entire grid, which reduces the computational complexity in determining the potential surface enormously.

In ref 4, the quantum—classical separation scheme in QWAIMD has been evaluated through computation of the vibrational spectrum of a strongly anharmonic hydrogen-bonded system. The main features of these results are summarized in Appendix A. In addition, as noted in the Introduction, QWAIMD has been adopted to study hydrogen tunneling in enzyme-active sites,[7,24] and QM/MM generalizations to the TDDS implementation of QWAIMD have also been completed.[5] In ref 103, the quantum dynamics tools from QWAIMD were used to compute the qualitative accuracy involved in classical ab initio molecular dynamics calculations of vibrational spectra in hydrogen-bonded systems.

While the classical equations of motion above can automatically be applied for periodic electronic systems,[104] in the next few sections, we undertake generalizations to the quantum propagator in eq 1 to facilitate the treatment of extended systems.

3. EXTENDED SYMMETRIZED DISTRIBUTED APPROXIMATING FUNCTIONAL PROPAGATOR (ESDAF-P) FORMALISM

As noted above, the quantum dynamical propagation in QWAIMD is carried out through a Trotter symmetric factorization

$$\psi(x_i; t) = \sum_j \exp\left\{-\frac{iV(x_i; t)t}{2\hbar}\right\} \tilde{K}(x_i, x_j; t)$$

$$\exp\left\{-\frac{iV(x_j; t)t}{2\hbar}\right\} \psi(x_j; 0) \qquad (11)$$

where $\tilde{K}(x_i, x_j; t)$ is the DAF representation of the free propagator on Cartesian grids shown in eq 1 and $V(x; t)$ is the electronic structure potential energy computed on-the-fly. For cases where the wavepacket $\psi(x_j; 0)$ is known to possess symmetry on account of the potential $V(x; t)$, as in the extended systems to be treated here, we may utilize such symmetry to adapt the propagation scheme. Hence, as a first step, nuclear coordinate transformations are introduced in section
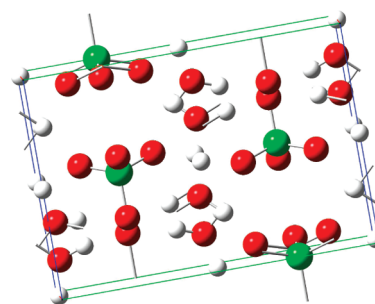

Figure 2. Rectangular unit cell of aquonium perchlorate, $H_5O_2ClO_4$, with four formula units. Unit cell dimensions are 5.79, 10.98, and 7.33 Å, with all unit cell angles equal to 90°.

IIIA. These transformations utilize the symmetry of the potential to derive coordinate transformations that result in collective nuclear modes that obey the crystal symmetry. Once these symmetry transformations are outlined, in section IIIB, we obtain general expressions for the free propagator acting on functions with periodic boundary conditions.

A. Introducing Collective Nuclear Coordinates Using Projection Operators. In Figure 2, we present the aquonium perchlorate system that has been the subject of recent neutron scattering studies on account of its low-temperature protonic conductor properties.[27] Systems displaying the ability to allow transport of protons, that is, protonic and superprotonic conductors,[25−28,34] while retaining stability have application in the construction of solid-state fuel cells, gas sensors, and electronic displays. Furthermore, many similar periodic protonic conducting systems have also been found to display para-electric to ferroelectric or antiferroelectric transitions and nonlinear optical properties.

To study the quantum dynamics of the shared proton in such systems, we first note that the mass-weighted position of a proton in the primary unit cell, designated as r_0, is related to protons in other unit cells of the supercell (r_i) by the transformation

$$\mathscr{R}_i r_0 \equiv r_i \qquad (12)$$

If L is the length of the supercell, containing $N_{\mathscr{G}}$ unit cells, then the domain of definition of the position variables obeys $r_0 \in [0, L/N_{\mathscr{G}}]$, and $r_i \in [i * L/N_{\mathscr{G}}, (i + 1) * L/N_{\mathscr{G}}]$. The quantity $\mathscr{R}_i$ is a transformation operator, which could be a translation or a reflection operation that connects the two coordinates. All such operations, $\{\mathscr{R}_i\}$, form a group, $\mathscr{G}$, which now contains $N_{\mathscr{G}}$ elements. [Note that the supercell defines the size of the problem in real space about which the wave function is completely periodic, whereas $N_{\mathscr{G}}$ represents the number of unit cells inside of the supercell, about which the wave function obeys Bloch symmetry.]

The Hamiltonian for this system is

$$-\frac{1}{2}\sum_{i=1}^{N_{\mathscr{G}}} \nabla_i^2 - \frac{1}{2}\sum_{I=1}^{N_H} \nabla_I^2 + H_e \qquad (13)$$

where the number of protons in the supercell is assumed to be the same as the number of unit cells in the supercell and N_H represents the number of heavy nuclei in the system. The operator H_e is the electronic Hamiltonian, which is a function of the electronic coordinate, r_e, the associated momenta, and the electron nuclear potential, $V(\{\tilde{r}_i, \tilde{r}_I\}; \{r_e\})$. The quantities $\{\tilde{r}_i, \tilde{r}_I\}$ represent the nuclear coordinates without mass-weighting. In the discussion below, the heavy atom nuclei are assumed to obey classical mechanics.

We next introduce a symmetry-governed coordinate transformation for the light nuclei

$$\mathbf{s}_\mu \equiv \sqrt{\frac{1}{N_\mathscr{G}} \sum_{i=0}^{N_\mathscr{G}-1} \Gamma^\mu(\mathscr{R}_i)\{\mathscr{R}_i \mathbf{r_0}\}}$$

$$= \sqrt{\frac{1}{N_\mathscr{G}} \sum_{i=0}^{N_\mathscr{G}-1} \Gamma^\mu(\mathscr{R}_i)\mathbf{r_i}} \tag{14}$$

where $\{\Gamma^\mu\}$ are a set of irreducible representation transformation matrices that represent the operations in the group, $\mathscr{G}$. For the case where all of the $\{\mathscr{R}_i\}$ commute, the irreducible representations are one-dimensional, and $\Gamma^\mu \equiv \chi^\mu$, the characters of the individual irreducible representations. In general, $\chi^\mu = \mathrm{Tr}[\Gamma^\mu]$. Furthermore, while $\mathbf{r_i} \in [i*L/N_\mathscr{G}, (i+1)*L/N_\mathscr{G}]$, $\mathbf{s}^\mu \in [0,L]$. In this transformed coordinate system, the Laplacian, $\nabla_i^2 \equiv \nabla_i \cdot \nabla_i$, in eq 13, with gradients given by

$$\nabla_i = \sum_{\nu=1}^{N_\mathscr{G}} \Gamma^\nu(\mathscr{R}_i)\nabla_{\mathbf{s}_\nu} \tag{15}$$

may be written as

$$\nabla_i^2 = \nabla_i \cdot \nabla_i = |\nabla_i|^2$$

$$= \sum_{\mu,\nu=1}^{N_\mathscr{G}} \left[\frac{1}{N_\mathscr{G}}\Gamma^\mu(\mathscr{R}_i)*\Gamma^\nu(\mathscr{R}_i)\right]\nabla_{\mathbf{s}_\mu} \cdot \nabla_{\mathbf{s}_\nu} \tag{16}$$

For complex $\Gamma^\nu(\mathscr{R}_i)$, a complex conjugate is introduced on the left gradient operator of the Laplacian to maintain the coefficients of the sum on the right side of eq 16 as real. This is no different from introducing a complex conjugation in the dual vector space while computing expectation values in quantum mechanics. The Hamiltonian in eq 13 then takes the form

$$H = -\frac{1}{2}\sum_{\mu,\nu=1}^{N_\mathscr{G}} \left[\frac{1}{N_\mathscr{G}}\sum_{i=1}^{N_\mathscr{G}} \Gamma^\mu(\mathscr{R}_i)*\Gamma^\nu(\mathscr{R}_i)\right]\nabla_{\mathbf{s}_\mu} \cdot \nabla_{\mathbf{s}_\nu}$$
$$- \frac{1}{2}\sum_{i=1}^{N_\mathrm{H}} \nabla_i^2 + H_\mathrm{e} \tag{17}$$

Using, now, the "Great orthogonality relation"[105] reduces the bracketed quantity, $[\cdots]$, in the above equation to $\delta_{\mu,\nu}$. In other words, this reduces the metric tensor for the transformation in eq 14 to the diagonal form, and eq 17 reduces to

$$H = -\frac{1}{2}\sum_{\mu=1}^{N_\mathscr{G}} \nabla_{\mathbf{s}_\mu}^2 - \frac{1}{2}\sum_{i=1}^{N_\mathrm{H}} \nabla_i^2 + H_\mathrm{e} \tag{18}$$

In other words, the symmetry-governed coordinate transformation in eq 14 is a unitary transformation. The time-dependent Schrödinger equation corresponding to the Hamiltonian in eq 18 is then simplified by assuming a quantum−classical separation of the light and heavy nuclei and electrons. Here, the light nuclei as well as the electrons are treated quantum mechanically, while the heavier nuclei are treated classically. This yields[1] a classical equation for the heavy nuclei, a time-independent single-particle equation for the electrons, and a time-dependent Schrödinger equation for the collective variables, $\mathbf{s}_\mu$

$$i\hbar\frac{\partial}{\partial t}\psi_{\mathbf{s}_\mu}(\mathbf{s}_\mu;t) = H_{\mathbf{s}_\mu}\psi_{\mathbf{s}_\mu}(\mathbf{s}_\mu;t) \tag{19}$$

where $H_{\mathbf{s}_\mu} \equiv \langle\psi_\mathrm{H}\psi_\mathrm{e}|H|\psi_\mathrm{H}\psi_\mathrm{e}\rangle$; ψ_H is a delta-function that represents the position of the classically treated heavy nuclei and ψ_e is the

electronic wave function. The electronic degrees of freedom are coupled to the motion of light and heavy nuclei through a potential that depends on the light nuclear time-dependent wavepacket and heavy atom coordinates.

We now provide relations that transform the single-particle functions, $f_i(\tilde{\mathbf{r}}_i)$, to functions associated with the collective variable $\mathbf{s}_\mu$. Toward this, we introduce a set of operations $\{O\mathscr{R}_i\}$ that are isomorphic[105] to the set $\{\mathscr{R}_i\}$ but differ on the basis that each $O\mathscr{R}_i$ acts on a function as opposed to a real-space variable. Following this, we introduce projection operators[105]

$$\mathscr{P}^\mu \equiv \sqrt{\frac{1}{N_\mathscr{G}} \sum_{\mathscr{R}_i \in \mathscr{G}} \Gamma^\mu(\mathscr{R}_i)O_{\mathscr{R}_i}}$$

$$= \sqrt{\frac{1}{N_\mathscr{G}} \sum_{i=0}^{N_\mathscr{G}-1} \Gamma^\mu(\mathscr{R}_i)O_{\mathscr{R}_i}} \tag{20}$$

that act on $f_i(\tilde{\mathbf{r}}_i,t)$ to create $f^\mu(\mathbf{s}_\mu,t)$ according to

$$f^\mu(\mathbf{s}_\mu,t) = \mathscr{P}^\mu f_0(\mathbf{r}_0,t)$$

$$= \sqrt{\frac{1}{N_\mathscr{G}} \sum_{i=0}^{N_\mathscr{G}-1} \Gamma^\mu(\mathscr{R}_i)O_\mathscr{R} f_i(\mathbf{r_0},t)}$$

$$= \sqrt{\frac{1}{N_\mathscr{G}} \sum_{i=0}^{N_\mathscr{G}-1} \Gamma^\mu(\mathscr{R}_i)f_i(\mathscr{R}_i\mathbf{r_0},t)}$$

$$= \sqrt{\frac{1}{N_\mathscr{G}} \sum_{i=0}^{N_\mathscr{G}-1} \Gamma^\mu(\mathscr{R}_i)f_i(\mathbf{r_i},t)} \tag{21}$$

Equation 21 is to be interpreted as follows. The quantities $f_i(\mathbf{r_i},t)$ represent functions appropriate for each protonic coordinate, that is, they are single-particle functions. Each proton only has coordinates inside of a box of length $L/N_\mathscr{G}$. The functions $f^\mu(\mathbf{s}_\mu,t)$ depend on the variable $\mathbf{s}_\mu$, which extends right through the supercell. The values of these functions outside of a primary unit cell are determined based on symmetry, as given in eq 21. It may be noted that the projection operators defined in eq 20 were also used o define the coordinate transformation in eq 14, that is, $\mathbf{s}_\mu \equiv \mathscr{P}^\mu\mathbf{r}_0$.

B. Quantum Dynamical Propagation of Functions of $\mathbf{s}_\mu$. We next derive a quantum evolution of the wave function given in eq 19. The formulation includes the full symmetry of the crystal.

From the continuous generalization of eq 2, the free propagation of a general function, $f(x;t)$, defined from $-\infty$ to $+\infty$, is given by the action of the propagator $\tilde{K}(x_i,x_j;t)$ as

$$f(x,t) = \int_{-\infty}^{+\infty} \tilde{K}(x,x';t)f(x';t=0)\,dx' \tag{22}$$

Here, we utilize the generic variable x to depict the transformed coordinate $\mathbf{s}_\mu$ introduced in the previous section. The numerical portion of this paper is focused toward the choice $\tilde{K}(x_i,x_j;t) \equiv \tilde{K}(x-x';t)$, from eq 1. However, the recipe provided in this section for propagator symmeterization is general, and hence, we first contrast three different choices for the propagator, $\tilde{K}(x_i,x_j;t)$. The first choice that we consider here is the one obtained from fast Fourier transforms.[51,53−57] In this case, the free propagator

E

dx.doi.org/10.1021/jp112389m |*J. Phys. Chem. A* XXXX, XXX, 000−000

may be written as

$$\left\langle x \left| \exp\left\{ -\frac{iK\Delta t}{\hbar} \right\} \right| x' \right\rangle \equiv \int dk \left\langle x \left| \exp\left\{ -\frac{iK\Delta t}{\hbar} \right\} \right| k \right\rangle \left\langle k \middle| x' \right\rangle$$

$$= \int dk \, \exp[ik(x-x')] \exp\left\{ -\frac{i\hbar k^2 \Delta t}{2m} \right\} = (1-i)\sqrt{\frac{m\pi}{\hbar\Delta t}} \exp\left\{ \frac{im(x-x')^2}{2\Delta t\hbar} \right\}$$

(23)

Clearly, this is a highly oscillatory function of $(x - x')$, and in fact, as $(x - x')$ increases and/or Δt decreases, the oscillation frequency also increases. Finite, fast Fourier transforms are often used to partially alleviate this problem. The second approach that we note here is the Bessel−Chebychev expansion derived from the Jacobi−Anger formula[66]

$$\exp(-izx) = \sum_{n=0}^{\infty} (2 - \delta_{n,0})(-i)^n J_n(z) T_n(x) \quad (24)$$

and hence

$$\exp(-iH_{norm}t/\hbar) = \sum_{n=0}^{\infty} (2 - \delta_{n,0})(-i)^n J_n(t) T_n(H_{norm}) \quad (25)$$

where H_{norm} is the normalized Hamiltonian, $H_{norm} = (H - \bar{H})/(\Delta H)$, with $\bar{H} = (1/2)(H_{max} + H_{min})$ and $\Delta H = (1/2)(H_{max} - H_{min})$. The quantities H_{max} (H_{min}) are the maximum (minimum) eigenvalues of the truncated, finite matrix approximation to the Hamiltonian.[106] The quantities $\{T_n(x)\}$ are the Chebychev polynomials of the first kind, and $J_n(z)$ are the cylindrical Bessel functions. In the cases listed above, it is possible to write $\tilde{K}(x_i, x_j; t) \equiv \tilde{K}(x - x'; t)$, and thus, eq 22 may be rewritten as

$$f(x, t) = \int_{-\infty}^{+\infty} \tilde{K}(x - x'; t) f(x'; t = 0) \, dx' \quad (26)$$

Because eq 26 defines a general time-dependent convolution relation, the analysis below applies to all such operations, including Green's functions.

If the function $f(x,t)$ is periodic, that is, $f(x \pm mL; t) = f(x; t)$ for all integer values of m, then its quantum dynamical evolution may be written as

$$f(x; t) = \int_0^L \mathcal{K}_{\mathcal{P}}(x - x'; t) f(x'; t = 0) \, dx' \quad (27)$$

where

$$\mathcal{K}_{\mathcal{P}}(x - x'; t) = \sum_{n=-\infty}^{+\infty} \tilde{K}(x - x' + nL; t) \quad (28)$$

is the free quantum propagator, adapted to the periodic symmetry of the wavepacket $f(x; t=0)$. The banded nature of the DAF representation (see eq 1) reduces the infinite summation in eq 28 to a finite summation up to a (small) integer n_0. Thus, in practice

$$\mathcal{K}_{\mathcal{P}}(x - x'; t) = \sum_{n=-n_0}^{n_0} \tilde{K}(x - x' + nL; t) \quad (29)$$

For a discrete grid, the integral in eq 27 can be approximated through the Trapezoidal rule or other approximations to numerical quadrature. In this publication, we adopt the Trapezoidal approach.

Equation 27 describes the evolution of a state that obeys periodic boundary conditions (PBC). The symmetry is enforced

by the potential. The variable, x, as stated earlier, refers to transformed coordinate variables obtained in the previous section. In such cases, additional symmetry may also be present. That is, as in the previous section, consider a set of operations, $\{\mathcal{R}_i\}$, that belong to the group $\mathcal{G}$. Let the group $\mathcal{G}$ contain $N_{\mathcal{G}}$ operations. If the function $f(x,t)$ in eq 27 conforms to the symmetry of $\mathcal{G}$, then there exists a symmetry operation $\mathcal{R}_i \in \mathcal{G}$ such that for every $y' \in [0, L/N_{\mathcal{G}}]$, there exists $\mathcal{R}_i y' = x'$, where $x' \in [(iL)/(N_{\mathcal{G}}), ((i + 1)L)/(N_{\mathcal{G}})]$. That is, if $L/N_{\mathcal{G}}$ is the length of a one-dimensional unit cell and L is the corresponding supercell, y' is a point belonging to the primary unit cell (corresponding to the $\mathbf{r}_0$ variable used in the previous section), and x' belongs to the supercell (corresponding to the $\mathbf{r}_i$ variable used in the previous section). If we now assume that the initial wavepacket, $f(x'; t=0)$ in eq 27, belongs to the μth irreducible representation of $\mathcal{G}$, that is, $f(x'; t=0) \equiv f^\mu$, then the propagated wavepacket, projected onto the νth irreducible representation is

$$\underline{\mathcal{P}^\nu\{f(x; t)\}} = \mathcal{P}^\nu\left\{ \int_0^L \mathcal{K}_{\mathcal{P}}(x - x'; t) \mathcal{P}^\mu \underline{\mathcal{P}^\mu f(x'; t = 0)} \, dx' \right\} \quad (30)$$

where the underbrace depicts the projected states. Furthermore, we have used the fact that the projection operators are idempotent,[105] that is $\mathcal{P}^\mu \mathcal{P}^\mu \equiv \mathcal{P}^\mu$. Using the definition of the projection operator given in eqs 20 and 21, the above equation reduces to

$$f^\nu(x; t)$$

$$= \int_0^L [\mathcal{P}^\nu \mathcal{K}_{\mathcal{P}}(x - x'; t) \mathcal{P}^\mu] \left\{ \sqrt{\frac{1}{N_{\mathcal{G}}}} \sum_{\mathcal{R}_i \in \mathcal{G}} \Gamma^\mu(\mathcal{R}_i) f(\mathcal{R}_i x'; t = 0) \right\} dx'$$

$$= \int_0^L \left[\frac{1}{N_{\mathcal{G}}} \sum_{\mathcal{R}_i, \mathcal{R}'_i \in \mathcal{G}} \Gamma^\nu(\mathcal{R}_i) \mathcal{K}_{\mathcal{P}}(\mathcal{R}_i x - \mathcal{R}'_i x'; t) \Gamma^\mu(\mathcal{R}'_i) \right]$$

$$\times \left\{ \sqrt{\frac{1}{N_{\mathcal{G}}}} \sum_{\mathcal{R}_i \in \mathcal{G}} \Gamma^\mu(\mathcal{R}_i) f(\mathcal{R}_i x'; t = 0) \right\} dx' \quad (31)$$

Now, because, by definition, $\mathcal{R}_i y' = x'$, and the set of operations, $\mathcal{R}_i \in \mathcal{G}$, form a group, there always exists an operation, $\mathcal{R}'_i \in \mathcal{G}$, such that $\mathcal{R}'_i x' = y'$. Thus, in the above expression, $\{x, x' \in [0, L]\}$, and $\{\mathcal{R}_i x, \mathcal{R}'_i x' \in [0, L/N_{\mathcal{G}}]\}$. Using the change of variables, $\mathcal{R}'^{-1}_i y' = x'$, which implies $\{[\mathcal{R}'^{-1}_i dy'] = dx'\}$, and $y' \in [0, L/N_{\mathcal{G}}]$ while $x' \in [0, L]$, we obtain

$$f^\nu(y; t) = \int_0^{L/N_{\mathcal{G}}} \mathcal{K}_{\mathcal{P}}^{\nu,\mu}(y - y'; t) f^\mu(y'; t = 0) \, dy' \quad (32)$$

where

$$\mathcal{K}_{\mathcal{P}}^{\nu,\mu}(y - y'; t)$$

$$= \frac{1}{N_{\mathcal{G}}} \sum_{\mathcal{R}_i, \mathcal{R}'_i \in \mathcal{G}} \Gamma^\nu(\mathcal{R}_i) \mathcal{K}_{\mathcal{P}}(\mathcal{R}_i x - \mathcal{R}'_i x'; t) \Gamma^\mu(\mathcal{R}'_i)$$

(33)

and

$$f^\mu(y'; t = 0) = \sqrt{\frac{1}{N_{\mathcal{G}}}} \sum_{\mathcal{R}_i \in \mathcal{G}} \Gamma^\mu(\mathcal{R}_i) f(\mathcal{R}_i x'; t = 0) \quad (34)$$

Note that in eq 32, the domain of the definition of the function in real space has been reduced to the size of the unit cell as opposed to

the supercell. [Compare with eq 27.] Thus, eq 33 yields the general expression for the extended symmetrized distributing approximating functional propagator (ESDAF-P) when the DAF free propagator in eq 1 is used for $\tilde{K}(x-x';t)$.

1. Dimensionality of Γ^μ. We introduced general expressions for the ESDAF-P propagator above. The numerical implementation of the expressions depends on the form of the Γ^μ transformation matrices. As we noted previously, when all of the $\{\mathcal{R}_i\}$ commute, $\Gamma^\mu \equiv \chi^\mu$, the characters of the individual irreducible representations. The corresponding expression for the ESDAF-P propagator is simply

$$\mathcal{K}_{\mathscr{P}}^{\nu,\mu}(y - y'; t)$$

$$= \sum_{\mathcal{R}_i, \mathcal{R}'_i \in \mathscr{G}} \sqrt{\frac{1}{N_{\mathscr{G}}}} \chi^{\nu*}(\mathcal{R}_i) \mathcal{K}_{\mathscr{P}}(\mathcal{R}_i x - \mathcal{R}'_i x'; t) \chi^\mu(\mathcal{R}'_i) \sqrt{\frac{1}{N_{\mathscr{G}}}} \quad (35)$$

and χ^μ replaces Γ^μ in eq 34. However, when operations in $\mathscr{G}$ do not commute with each other (non-Abelian groups), the Γ^μ irreducible representations may be multidimensional. In such cases, one case still uses eq 35 with $\chi^\mu = \text{Tr}[\Gamma^\mu]$. However, if the initial wavepacket belongs to the jth column of the μth irreducible representation of $\mathscr{G}$, the full transformation matrix, Γ^μ, can be used as

$$f(y'; t = 0) \equiv f_j^\mu(y'; t = 0)$$

$$= \sqrt{\frac{l_\mu}{N_{\mathscr{G}}}} \sum_{\mathcal{R}_i \in \mathscr{G}} \Gamma_{j,j}^\mu(\mathcal{R}_i) f(\mathcal{R}_i x'; t = 0) \quad (36)$$

where l_μ is the dimensionality of the μth irreducible representation. The form of the ESDAF-P propagator in this case is

$$\mathcal{K}_{\mathscr{P}}^{(\nu,j);(\mu,j)}(y - y'; t)$$

$$= \frac{\sqrt{l_\nu l_\mu}}{N_{\mathscr{G}}} \sum_{\mathcal{R}_i, \mathcal{R}'_i \in \mathscr{G}} \Gamma_{j,j}^\nu(\mathcal{R}_i) \mathcal{K}_{\mathscr{P}}(\mathcal{R}_i x - \mathcal{R}'_i x'; t) \Gamma_{j,j}^\mu(\mathcal{R}'_i)$$

$$(37)$$

Although, in principle, any quadrature scheme (e.g., Monte Carlo quadrature or any uneven grid) can be used to approximate the integrals above; the results from a discrete representation of the integrals using extended trapezoidal rule are used in this publication.

4. RESULTS AND DISCUSSION

There are two sets of symmetry operations and, consequently, two kinds of groups in crystals, (1) point group symmetry operations (rotation and reflection) and (2) translational operations along the Bravais lattice. Furthermore, the crystallographic point group must comply to the extension of the crystal lattice, that is, the rotation and reflection operations in the point group must keep the Bravais lattice invariant. This additional property separates the space groups into two categories: (a) When the point group operations and the translation group are separable, the space group is a semidirect product of the two subgroups comprised of these operations. In this case, the space group is called symmorphic. (b) When the point group and translation group are nonseparable, that is, when a glide reflection or a screw rotation is involved, the space group is nonsymmorphic. The formalism outlined in the previous section is general and includes both kinds of groups; however, in the numerical portion of this

Table 1. Simulation Details for the Free-Particle Benchmarks

dimensionality[a]	k-values[b]	number of irreps[c]	N_g[d]
1D[e]	4	4	10^2
	8	8	10^2
	16	16	10^2
	32	32	10^2
	64	64	10^2
	128	128	10^2
2D[e]	4×4	10	10^4
	8×8	36	10^4
	16×16	136	10^4
	32×32	528	10^4
3D[e]	$4 \times 4 \times 4$	4	10^6
	$8 \times 8 \times 8$	8	10^6
	$16 \times 16 \times 16$	12	10^6

[a] The kinetic energy operator as well as the free propagator in multiple dimensions are constructed through direct product. [b] In higher dimensions, the **k** space is symmetric, that is, $k_x^{max} = k_y^{max} = k_z^{max}$ in 3D. [c] Number of irreducible representations. [d] Number of grid points inside of a unit cell. Equal in each dimension. [e] Unit cell length in each dimension: $l = \pi/2$ au. Grid discretization in each dimension: $\Delta = 0.0157$ au.

paper, we benchmark the development for symmorphic group representation of ESDAF-P. The study of nonsymmorphic space groups will be part of future studies.

In this section, we benchmark the accuracy and efficiency of the ESDAF-P formalism for both proton and electron dynamics in extended systems. In section IVA, a free-particle state obeying periodic boundary conditions is considered. Here, the wave function outside of the unit cell is obtained using Bloch symmetry

$$\Psi(\mathbf{r} + \mathbf{T}) = \exp\{i\mathbf{k}\cdot\mathbf{T}\}u(\mathbf{r}) u(\mathbf{r} + \mathbf{T}) = u(\mathbf{r}) \quad (38)$$

where $\mathbf{k} \equiv [k_x, k_y, k_z]$ is a momentum space (or reciprocal space) vector and $\mathbf{T}$ is the unit cell translation vector. The ESDAF-P formalism is tested for large values of the reciprocal space index, **k**, in section IVA. In all cases, the formalism is shown to provide good accuracy and efficiency. In section IVB, the periodic system of section IVB is perturbed to represent the dynamics of a single-particle electronic state in a crystal lattice. As such, the studies in section IVB may be considered akin to a time-dependent density-functional-type treatment of a periodic electronic system beyond linear response.[10,11,107,108] Section IVC includes the study of proton dynamics in a two-dimensional extended lattice. The system chosen here is a concentrated low-temperature lattice of hydrochloric acid in water, $[H(H_2O)_4^+/C^-]_{n=\infty}$, which is derived from the proposed structural motif,[109] $H(H_2O)_6^+/C^-$, for concentrated hydrochloric acid solution. This structure is thought to be consistent with the X-ray measurements and neutron scattering data.[109] The hydrogen bonding network in the structure facilitates protonic conduction in the presence of an external field.

A. Quantum Dynamical Propagation of a Single Free-Particle State Obeying Periodic Boundary Conditions (PBC). We propagate various linear combinations of eigenstates of the momentum operator, $\exp\{ikx\}$, where $k = (2m\pi)/(Nl)$ and $m = 0, 1, 2, ..., N - 1$ to demonstrate the accuracy of the ESDAF-P formalism. We have tested the performance in propagating initial states for systems with large **k** values, as discussed in Table 1. Specifically, we
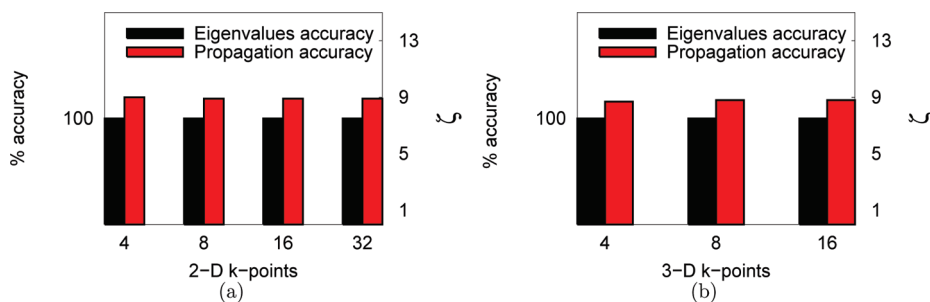
Figure 3. Accuracy of ESDAF-P for 2D (a) and 3D (b) free-particle states. In both figures, the left vertical axis represents the percentage of eigenvalues with accuracy $\epsilon > 10$ (see eq 41). The right axis represents the propagation accuracy ζ defined in eq 45. (See text for details.)

first utilize an extended symmetrized form of the kinetic energy operator (see below) to obtain a set of eigenstates of chosen symmetry. We then construct an initial wavepacket from a collection of these eigenstates, to be propagated using ESDAF-P. The unit cell dimensions, grid discretization parameters, and information regarding irreducible representations are provided in Table 1.

To represent the kinetic energy operator, we consider the following general form of the DAF for propagation and differentiation[1,2,81−84,88,110]

$$\tilde{K}_{N_{der}}(x_i - x_j; \Delta t) = \frac{1}{\sigma(0)\sqrt{2\pi}}\left(\frac{-1}{\sqrt{2}\sigma(0)}\right)^{N_{der}} \exp\left(-\frac{(x_i - x_j)^2}{2\sigma(\Delta t)^2}\right)$$

$$\times \sum_{n=0}^{M/2}\left(\frac{\sigma(0)}{\sigma(\Delta t)}\right)^{2n+1}\left(\frac{-1}{4}\right)^n \frac{1}{n!}H_{2n+N_{der}}\left(\frac{x_i - x_j}{\sqrt{2}\sigma(\Delta t)}\right) \quad (39)$$

where $\{\sigma(\Delta t)\}^2 = \sigma(0)^2 + (i\Delta t\hbar/m)$, Δt is the propagation time step, and $H_{2n+N_{der}}(x)$ are Hermite polynomials of order $2n + N_{der}$. Equation 39 is a generalization of eq 1 and includes both the free propagation and differentiation. For example, eq 39 represents a formally exact representation of the quantum dynamical free propagator[2,81,88] for $N_{der} = 0$, as noted earlier, and also represents a second-derivative operator, and hence the kinetic energy operator, when $N_{der} = 2$ and $\Delta t = 0$.[1,2,82,91] As in the case of eq 1, eq 39 also provides a banded, sparse, Toeplitz representation. Equation 39 is utilized in place of $\mathscr{K}$ in eqs 28, 33, 35, and 37 to obtained extended-symmetrized versions of both the quantum propagator and derivative operators. The particle mass is chosen to be the hydrogen mass, $m = 1836.2$ au.

The characters for the irreducible representations of the translation group are $\{\exp\{iqn2\pi/N\}\}$, for $n = 0, ..., N - 1$ and $q = 0, ..., N - 1$. Here, q labels the irreducible representation, n labels the translation vector, and N is the number of unit cells inside of the supercell. Using these characters in eqs 28, 33, 35, and 37, we arrive at the discretized version of ESDAF-P for the propagator and kinetic energy operator as

$$\mathscr{K}_{\mathscr{G}-C_N}^q(x_i, x_j; t) = \Delta x\left[\sum_{n=0}^{N-1}e^{iqn2\pi/N}\mathscr{K}_{\mathscr{P}}(x_i - x_j - nL/N; t)\right] \quad (40)$$

This allows efficient construction of the Hamiltonian and also the quantum propagator. The Hamiltonian and the propagator in multiple dimensions are constructed through direct product. We obtain eigenstates for the symmetrized Hamiltonian by employing the Arnoldi iterative diagonalization scheme.[111−113] The Arnoldi scheme is a variant of the Lanczos procedure[112] and involves the

repetitive application of the Hamiltonian matrix on an initial vector to form a Krylov basis set.[112] The representation of the Hamiltonian in this new basis set leads to a Hessenberg form (tridiagonal form for symmetric matrices)[112] for the Hamiltonian matrix, which is relatively easy to diagonalize and is used to obtain a subset of eigenstates. The action of the Hamiltonian matrix on any vector is calculated by taking full advantage of the banded, sparse, Toeplitz structure of eq 39, as described in the appendix of ref 11.

For each ESDAF-P calculation adapted with a particular irreducible representation, we obtained the first 80, 50, and 30 lowest-energy eigenstates in one, two, and three dimensions respectively. We evaluated the accuracy of the eigenstates by calculating the quantity

$$\epsilon = -\log_{10}\left(\frac{|E_{ESDAF} - E_{exact}|}{|E_{exact}|}\right) \quad (41)$$

where E_{ESDAF} are the eigenvalues obtained from Arnoldi diagonalization of the ESDAF Hamiltonian and E_{exact} are the analytical solutions for the free-particle case. Utilizing the eigenstates for a given irreducible representation, μ, we construct a Boltzmann weighted initial wavepacket

$$|\psi(x; t = 0)\rangle = \sum_{i=1}^{N} c_i^\mu(0)|\phi_i\rangle_\mu = \exp\{-\beta E_i^\mu\}|\phi_i\rangle_\mu \quad (42)$$

where β is the inverse temperature. The error in numerical propagation is then computed using the $\mathscr{L}^2$ norm of the difference between the analytically propagated wavepacket

$$\exp\{-i\mathscr{K}t\}|\psi(x; t= 0)\rangle = \sum_{i=1}^{N} c_i^\mu(0)\exp\{-iE_i^\mu t\}|\phi_i\rangle_\mu \quad (43)$$

and the ESDAF-P propagated form

$$|\psi(x; t)\rangle_\mu^{DAF} = \sum_{i=1}^{N} c_{i,DAF}^\mu(t)|\phi_i\rangle_\mu \quad (44)$$

according to

$$\zeta = -\log_{10}\left(\frac{1}{T}\int_0^T dt \frac{1}{N}\sqrt{\sum_{i=1}^{N}|c_{i,DAF}^\mu - c_i^\mu(0)e^{-iE_i^\mu t}|^2}\right) \quad (45)$$

where T is the total propagation time.

In Table 2, we present the accuracy of one-dimensional ESDAF-P results. It is clear that about 48, 57, and 68% of the obtained eigenvalues are within 10^{-10}, 10^{-8}, and 10^{-6} accuracy
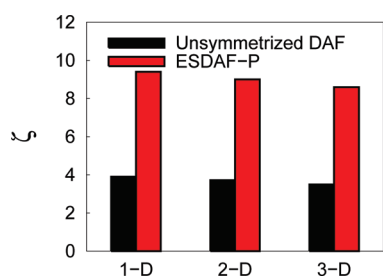
Figure 4. Effect of symmeterization through the use of eqs 28, 33, 35, and 37 on propagation accuracy. The quantity ζ is defined in eq 45.

Table 2. Accuracy of ESDAF-P for a 1D Free-Particle State

k-points	$N_{eig}{}^a$	$\epsilon > 10^b$	$\epsilon > 8^b$	$\epsilon > 6^b$	propagation accuracy^c
4	320	154	186	222	9.40
8	640	310	372	446	9.35
16	1280	620	746	890	9.34
32	2560	1240	1492	1780	9.34
64	5120	2480	2986	3560	9.34
128	10240	4962	5971	7120	9.34

^{a} Total number of eigenstates obtained. ^{b} Number of eigenvalues with accuracy ϵ (defined in eq 41) greater than 10, 8, and 6. ^{c} Propagation error calculated according to eq 45 and averaged over all of the calculations with different irreps. A temperature of 300 K is chosen to populate the initial wavepacket. (See eq 42.) The total propagation time is 100 fs with a time step of 0.01 fs. (The order of this time step is consistent with previous quantum/classical QWAIMD studies,[4,6] where the quantum nuclear time step is generally one order of magnitude smaller than the classical nuclear time step. The classical nuclear time step in QWAIMD is in turn restricted by the fact that on-the-fly electronic structure propagation is also performed within QWAIMD.)

for a range of **k**-points. Furthermore, the propagation of the wavepacket is also accurate through $\zeta \approx 10^{-9}$. In Figure 3a and b, we present the two- and three-dimensional ESDAF-P results. In higher dimensions, because only a small portion of the available eigenstates is acquired through Arnoldi diagonalization, all of the collected eigenvalues are accurate to 10^{-10}. The propagation error remains on the order of 10^{-9} all through. Again, the accuracies of eigenvalues and propagation remain independent of the choice of symmetry type. This is a clear indication of the robustness of ESDAF-P. In Figure 4, we compare the ESDAF-P results with those obtained in the absence of symmeterization. Here, the propagation accuracy using the regular DAF (that, is algorithms where eqs 1 and 39 are directly utilized without the symmeterization procedure in eqs 28, 33, 35, and 37) is compared with that obtained from ESDAF-P. It can be clearly seen that the accuracy of the ESDAF-P is generally 4 orders of magnitude superior.

In this section, we have utilized ESDAF-P to study the quantum dynamics of free-particle states obeying Bloch symmetry. It is shown that the ESDAF-P formalism is numerically accurate, efficient, and robust. To further test this formalism, in the next section, we study the quantum dynamics of a particle in a weak potential.

B. Weak Periodic Potential. Drude[114] used a classical free-particle description to study electrical conductivity and the Hall effect. In this model, the electron–electron interaction in the

Table 3. Accuracy of ESDAF-P for the Weak Perturbation Case

k-points	$N_{eig}{}^a$	$\epsilon > 10$	$\epsilon > 8$	$\epsilon > 6^b$	propagation accuracy^c
1	50	33	46	49	9.91
4	200	140	185	199	9.93
8	400	294	371	399	9.89
16	800	600	745	799	9.89
32	1600	1212	1491	1599	9.89
64	3200	2436	2983	3199	9.89
128	6400	4880	5965	6399	9.89

^{a} Total number of eigenvalues obtained. ^{b} Number of eigenvalues with $\epsilon > 6$ (eq 41). ^{c} Defined in eq 45. The error is averaged over all of the irreducible representations.

conduction band and the electron–ion interaction are neglected, and the valence electrons experience a constant periodic potential. In the previous section, we tested the ESDAF-P formalism to investigate the quantum dynamics of a free-particle state obeying PBC. In this section, this study is augmented by including a weak perturbing periodic potential. The nearly free particle model treated here has been successful in explaining electronic band gaps in crystals.[115] This is because the Coulomb interactions between the conduction band and the ions are shielded by the core electrons, giving rise to a smoother, weaker, periodic interaction potential.

The analytical solution to the quantum dynamics in the presence of a weak periodic potential is given in eq B10 in Appendix B and provides a rigorous test for ESDAF-P. Because the potential is periodic about the unit cell, that is, $V(x + l) = V(x)$, where l is the length of the unit cell, the potential may be expanded as a Fourier series $V(x) = \sum_n C_n \exp\{i2\pi n/l\}$. For our tests, the potential is chosen to be a linear combination of the kind

$$V(x) = A[\cos(4x) + \cos(8x) + \cos(12x) + \cos(16x)] \quad (46)$$

where $A = 10^{-3}$. This function has the property of being bound in the middle of a given unit cell, with repulsive barriers close to the edges. The oscillations in the bound region may represent interactions with ion cores. Because the potential is weak (by choice of the parameter $A = 10^{-3}$), eigenstates for the Hamiltonian can be obtained using perturbation theory, as discussed in Appendix B. These results are utilized to benchmark ESDAF-P.

We study the problem using **k**-point sampling with $N = 1, 4, 8, 16, 32, 64,$ and 128. The length of unit cell is chosen to be $l = \pi/2$ au, with 100 grid points in the unit cell and grid spacing of $\Delta = 0.018$ au. For each irreducible representation belonging to the chosen **k**, we obtain the first 50 lowest-energy eigenstates. The initial wavepacket is constructed as described in eq 42, and our results for accuracy in computing eigenvalues and propagation error are summarized in Table 3. It can be seen that both eigenvalue and propagation accuracies are of the same order as those for the free-particle case in the previous section.

To further probe the accuracy for different irreducible representations, we have analyzed the errors for the case of $N = 4$ in Table 4. To compare the ESDAF-P results with the perturbation treatment for a particular representation, we notice that there is a one-to-one correspondence between the free-particle wavevector k and the irreducible representation index q in eq 40. Utilizing the results from Appendix B, the eigenstates corrected to first

I

dx.doi.org/10.1021/jp112389m |*J. Phys. Chem. A* XXXX, XXX, 000–000

Table 4. Accuracy of ESDAF-P with k-Points $N = 4$ for the Weakly Perturbed Free-Electron Gas[a]

N_{Eig}[b]	$\epsilon > 10$[c]	$\epsilon > 8$	$\epsilon > 6$	ζ	N_{Eig}	$\epsilon > 10$	$\epsilon > 8$	$\epsilon > 6$	ζ
		$q = 0$					$q = 1$		
50	33	46	49	9.91	50	38	47	50	10.25
		$q = 2$					$q = 3$		
50	31	45	50	9.33	50	38	47	50	10.25

[a] Characters defined in eq 40. [b] Number of eigenstates acquired. [c] Number of eigenvalues with accuracy $\epsilon > 10, 8$, and 6 as defined in eq 41.

order can be written as

$$\phi_k = \frac{1}{\sqrt{Nl}} e^{ikx} + \sum_{n' = -\infty, n' \neq 0}^{\infty} \frac{\frac{1}{l}\left[\int_0^l e^{-in'x2\pi/l} V(x)\, dx\right]}{\frac{\hbar^2}{2m}\left[k^2 - \left(k + n'\frac{2\pi}{l}\right)^2\right]} e^{i(k + n'2\pi/l)x}$$

$$= \frac{1}{\sqrt{Nl}} e^{ikx}\left[1 + \sum_{n' = -\infty, n' \neq 0}^{\infty} \frac{\frac{1}{l}\left[\int_0^l e^{-in'x2\pi/l} V(x)\, dx\right]}{\frac{\hbar^2}{2m}\left[k^2 - \left(k + n'\frac{2\pi}{l}\right)^2\right]} e^{in'2\pi/lx}\right] \tag{47}$$

where $k = (2l\pi/Nl)$, $l = 0, \pm 1, \pm 2, ...$, is the wavevector of the single free-particle state obeying PBC and N is the value of the **k**-point sampling. It is straightforward to show that the wave function above has the Bloch symmetric form. Hence, in the weak perturbation scenario, the wavevector k is still a good quantum number. Thus, the index k can utilized to classify the states. Specifically, $k = (2(q + 4l)\pi)/(4l)$ ($q = 0, 1, 2, 3$; $l = 0, \pm 1, \pm 2$) corresponds to the qth irreducible representation for **k** value given by $N = 4$. The results are summarized in Table 4. The accuracy of calculations using different irreducible representations remain stable and accurate.

In sections IVA and IVB, we have benchmarked the ESDAF-P formalism for propagation by comparison to exact analytical results. In section IVB, the analytical result from Appendix B was used to benchmark the ESDAF-P results. It is, however, important to note that while the analytical treatment in Appendix B is only valid for weakly perturbative problems, on account of the use second-order perturbation theory, the ESDAF-P formalism is nonperturbative and is applicable to stronger perturbations as well. The accuracy limits on ESDAF-P, as already indicated in section IVA, may be governed by the choice of grid spacing commensurate with the rate of change of potential. Particularly, because the error in eq 11 is third order in intergration time step, with a prefactor that depends on the commutator of the kinetic and potential energy operators,[1,50−52] the intergration error in ESDAF-P is determined by the accuracy of the derivative of the potential on the grid. This places numerical bounds on the choice of the parameter A in eq 46 for a given spatial grid spacing. Of course, as the spatial grid spacing is further reduced, these restrictions disappear.

In the next section, further numerical benchmarks are provided, where we compute the vibrational spectrum of a protonic conductor using a novel velocity−flux correlation function (see ref 4 and eq 48 in the current publication). When such a flux formalism is used for the electronic dynamics case treated in this section and also treated in refs 10 and 11, one may treat the Hall conductance problem of conductivity orthogonal to the direction of electronic transport. This will be probed in future publications. In addition, the potential used in this section, namely, $V(x) = A[\cos(4x) + \cos(8x) + \cos(12x) + \cos(16x)]$, where $A = 10^{-3}$, has the property of being bound in the middle of a given unit cell, with repulsive barriers close to the edges. For such a potential, when the size of the unit cell is doubled and the wave function is periodic about this new unit cell, the barrier appears at the center of the new unit cell. In such cases, electron tunneling may occur. The quantum mechanical tunneling problem has already been well studied using QWAIMD in ref 7 for nuclear dynamics problems. The modification proposed here allows the treatment of tunneling in extended electronic systems (electron tunneling in nonequilibrium open systems has already been studied in refs 10 and 11) and will be pursued in future publications where the applications of the current formalism are discussed.

C. Quantum Dynamics of Collective Protonic Modes in Extended System. In this section, we provide preliminary results on the dynamical treatment of an extended protonic conducting system. As a benchmark of the ESDAF-P formalism, only the quantum dynamically treated collective modes corresponding to one excess proton per unit cell are studied here. Future studies will include the simultaneous time development of all other, classically treated nuclei in the periodic system, along with time-dependent treatment of the electronic structure as is customary in the quantum wavepacket ab initio molecular dynamics (QWAIMD) formalism.[1−11]

In ref 109, Agmon analyzed X-ray and neutron scattering data to propose a possible structural candidate to explain the 1:6 ratio of hydrochloric acid to water in concentrated hydrochloric solution. It was also hypothesized that this structure may polymerize to form a one-dimensional long-range ordered structure as indicated in Figure 5a and b. Optimization calculations using periodic boundary conditions and performed with the B3LYP density functional and double-ζ 6-31g(d) basis, implemented within the Gaussian suite of electronic structure codes, show that the unit cell length along the Cl−Cl direction is 8.60 Å, and that along the vertical oxygen−oxygen direction is 4.68 Å. While, in principle, all protons in this system can be studied using the formalism described here to simulate low-temperature dynamics, the collection of all transformations that incorporate both translational symmetry as well as internal symmetry in a unit cell form a nonsymmorphic group. As a first level of benchmark of the ESDAF-P formalism, we specialize here to symmorphic groups and hence only treat one proton inside of a unit cell quantum mechanically.

To study the collective modes of the shared proton in the vertical Zundel motif (see Figure 5b), the quantum dynamics of the shared proton is represented in a discrete Cartesian grid that is comprised of 300 grid points along each dimension. Using the time-dependent deterministic sampling (TDDS) algorithm discussed in refs 3, 4, and 9 with a summary provided in section IIA, the grid size is compressed to 441 points, which is the size of the set where electronic structure calculations were performed to
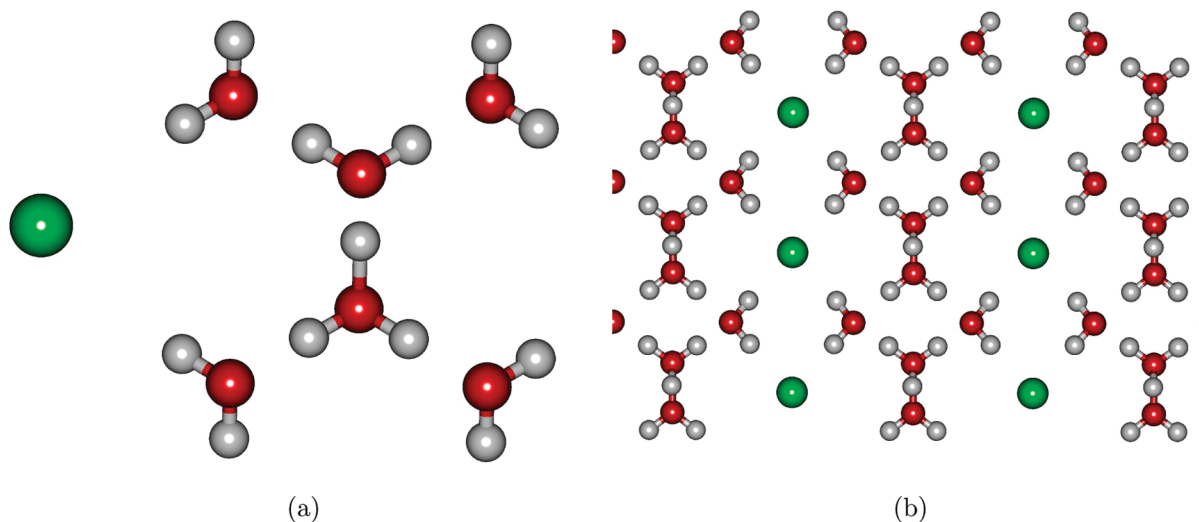
J

dx.doi.org/10.1021/jp112389m |*J. Phys. Chem. A* XXXX, XXX, 000–000

Figure 5. Periodic lattice structure for concentrated hydrochloric acid. (a) The structure proposed in ref 109 based on X-ray and neutron diffraction data. Note that the distance between the two oxygens in the Zundel cation $H_5O_2^+$ is 2.4 Å. (b) Optimized geometry of $H(H_2O)_4^+/Cl^-$ using DFT calculation with 2D PBC. The level of theory used in PBE with the 6-31g basis set. The lattice vector along the Cl—Cl direction is 8.06 Å, and that along the O—O direction is 4.68 Å. Green spheres depict the chlorine atoms, red spheres represent the oxygen atoms, and silver spheres denote hydrogen atoms.
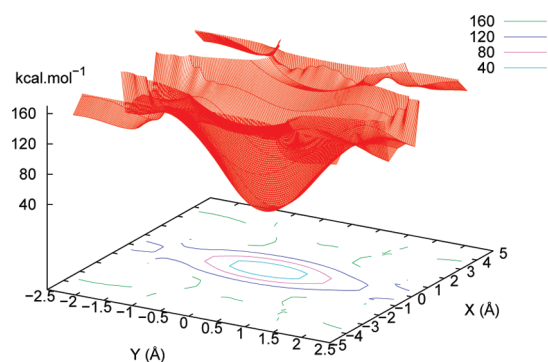

Figure 6. A two-dimensional potential surface for a shared proton in a periodic replicated lattice of $H(H_2O)_4^+Cl^-$ (see Figure 5b.) The surface is obtained using the PBE/3-21G level of theory with density fitting. The Y-direction represents the O—O distance.

obtain a potential surface. The potential values at the remaining grid points are obtained through Hermite curve interpolation.[102] Each potential energy value is obtained at the density functional theory (DFT), PBE/3-21g level of theory. The periodic electronic structure calculations performed to obtain this surface include **k**-point-sampling used with 12 electronic structure **k**-points along the Cl—Cl dimension and 18 along the vertical oxygen—oxygen direction. Thus, the total number of **k**-points used in each of the electronic structure calculations described below to obtain yjr surface is 216. Density fitting[116,117] was employed to accelerate the coulomb portion of the electronic calculations. The potential energy surface for the shared proton in the periodic $H(H_2O)_4^+/Cl^-$ system is shown in Figure 6. We obtained 10 eigenstates using the Arnoldi iterative diagonalization scheme[111−113] described earlier and constructed an initial wavepacket from a linear combination of the first 5 eigenstates, each carrying an equal weight. The wavepacket was then propagated using the ESDAF-P propagator.
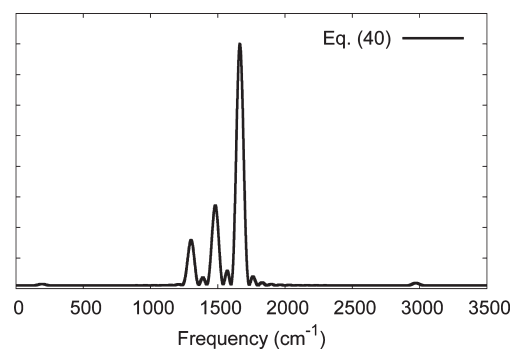

Figure 7. Fourier transform of the flux autocorrelation function generated using eq 48.

The vibrational properties corresponding to the propagated state were computed as in ref 4 (also see Appendix A) through introduction of the wavepacket flux autocorrelation function

$$C_J(\omega) = \int_{-\infty}^{+\infty} dt \, \exp[-i\omega t]\{\langle \mathbf{J}(t)\mathbf{J}(0)\rangle_Q\} \quad (48)$$

where the average flux, $\mathbf{J}(t)$, of the quantum wavepacket is

$$\mathbf{J}(t) = \langle \mathscr{J} \rangle = \mathscr{R}\left[\left\langle \psi(t)\left|\frac{-i\hbar}{m}\nabla\right|\psi(t)\right\rangle\right] \quad (49)$$

$\mathscr{R}[A]$ represents the real part of the complex number A. Equation 48 represents a reduced form of the velocity—flux autocorrelation function technique introduced in ref 4 to obtain quantum dynamical effects on vibrational spectral properties of potentially large systems.[5] The velocity—flux correlation function has been used in ref 4 to accurately compute vibrational properties in hydrogen-bonded systems. A rationalization for this
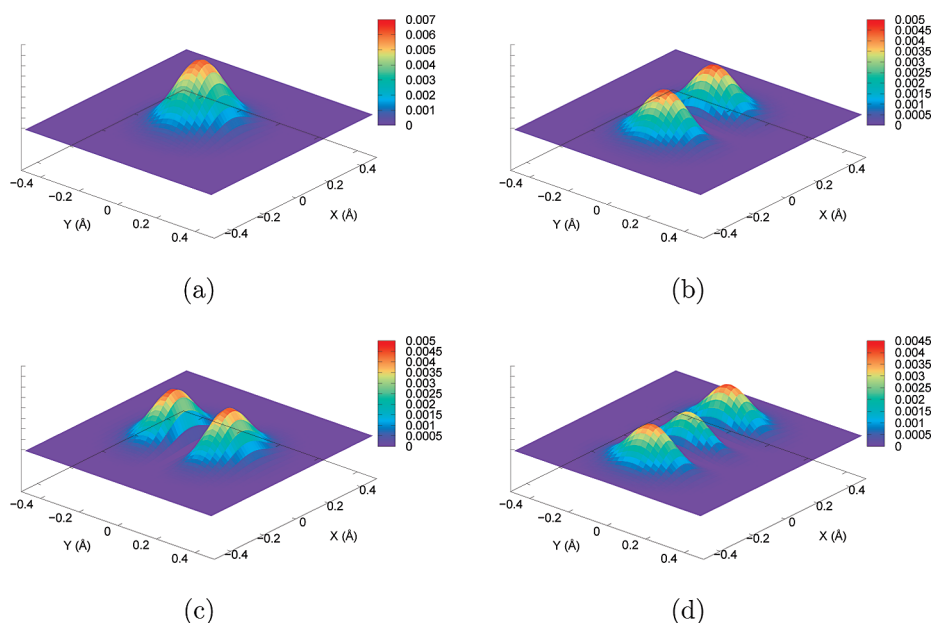
Figure 8. Ground through third excited state for the shared proton in the periodic $H(H_2O)_4^+/Cl^-$ system.

Table 5. Transition Frequencies and Dipole Intensities, $\langle\chi_i|\hat{x}|\chi_j\rangle$, for $H(H_2O)_4^+/Cl^-$ Using ESDAF-P[a]

FT-FAC (cm^{-1})	eigenvalues difference	transitions[b]	transition dipole moment
193.5	189.7	$2 \to 3$	0[c]
1302.4	1296.0	$3 \to 4$	0
1483.4	$\nu_{1\to2} = 1485.8$, $\nu_{2\to4} = 1485.8$[d]	$1 \to 2$ and $2 \to 4$	$d_{1\to2} = 0.12$, $d_{2\to4} = 0.24$
1664.3	$\nu_{1\to3} = 1675.5$, $\nu_{2\to5} = 1655.8$	$2 \to 5$ and $1 \to 3$	$d_{1\to3} = 0.012$, $d_{2\to5} = 0.012$
2973	2971.6	$1 \to 4$	0

[a] Based on the Nyquist−Shannon sampling theorem, the resolution in our analysis is 33 cm^{-1}. [b] The ground state starts with label 1. [c] The dipole transition moment less than 1.0×10^{-4} is shown to be zero. [d] Eigenvalue calculations show that these two transitions are degenerate.

expression can be found from the following set of arguments. In ref 4, it has been shown that for a time-independent Hamiltonian, H, the Fourier transform of the flux autocorrelation function is related to the vibrational properties through

$$\int_{-\infty}^{+\infty} dt \exp[-i\omega t]\{\langle \mathbf{J}(t)\mathbf{J}(0)\rangle_Q\} = \left|\int_{-\infty}^{+\infty} dt \exp[-i\omega t]\mathbf{J}(t)\right|^2$$

$$= \left|\int_{-\infty}^{+\infty} dt \exp[-i\omega t]\mathscr{R}\left[\sum_{i,j}\exp\left\{\frac{i(E_i - E_j)t}{\hbar}\right\}\frac{\langle\phi_i|\hat{\mathbf{p}}|\phi_j\rangle}{m}\right]\right|^2$$

$$= \left|\sum_{i,j}\delta\left(\omega - \frac{[E_i - E_j]}{\hbar}\right)\frac{\langle\phi_i|\hat{\mathbf{p}}|\phi_j\rangle}{m} + \delta\left(\omega - \frac{[E_j - E_i]}{\hbar}\right)\frac{\langle\phi_i|\hat{\mathbf{p}}|\phi_j\rangle^*}{m}\right|^2 \quad (50)$$

where E_i and ϕ_i are eigenvalues and eigenstates and $\hat{\mathbf{p}}$ is the momentum operator. Equation 50 indicates spectral peaks at eigenvalue differences, with intensities given by $\langle\phi_i|\hat{\mathbf{p}}|\phi_j\rangle$. On the other hand, the dipole intensities $\langle\chi_i\hat{x}\chi_j\rangle$ can be obtained in the harmonic limit using

$$\left\langle\chi_i\left|\frac{(\hat{\mathbf{a}} + \hat{\mathbf{a}}^\dagger)}{\sqrt{2m\omega}}\right|\chi_j\right\rangle = \frac{1}{\sqrt{2m\omega}}(\delta_{i,j=i-1} + \delta_{i,j=i+1}) \quad (51)$$

where χ_i are the eigenstates of the harmonic oscillator and $\hat{\mathbf{a}}^\dagger$ and $\hat{\mathbf{a}}$ are the creation and annihilation operators

$$\hat{\mathbf{a}} = \frac{1}{\sqrt{2}}\left(\sqrt{m}\omega\hat{\mathbf{x}} + i\frac{1}{\sqrt{m}}\hat{\mathbf{p}}\right)$$

$$\hat{\mathbf{a}}^\dagger = \frac{1}{\sqrt{2}}\left(\sqrt{m}\omega\hat{\mathbf{x}} - i\frac{1}{\sqrt{m}}\hat{\mathbf{p}}\right) \quad (52)$$

Along similar lines, in the harmonic limit

$$\langle\chi_i|\hat{\mathbf{p}}|\chi_j\rangle = \left\langle\chi_i\left|\frac{\sqrt{m}(\hat{\mathbf{a}} - \hat{\mathbf{a}}^\dagger)}{2i}\right|\chi_j\right\rangle$$

$$= \frac{\sqrt{m}}{2i}(\delta_{i,j=i-1} - \delta_{i,j=i+1}) \quad (53)$$

which provides similar selection rules as those corresponding to the transition dipole bracket in eq 51. It must be noted that the flux autocorrelation function in eq 48 has also been employed in refs 10 and 11 to compute the electrical conductivity through a molecular wire system that is connected to external probes.

Utilizing the general expression for the DAF in eq 39, with $N_{der} = 1$ and $\Delta t = 0$, that is, $\hat{K}_{N_{der}=1}(x_i - x_j; \Delta t=0)$ from eq 39, we

L

dx.doi.org/10.1021/jp112389m | J. Phys. Chem. A XXXX, XXX, 000–000

obtain the extended symmetrized flux operator as

$$
\begin{aligned}
\mathbf{J}(t) = \langle \mathscr{J} \rangle &= \mathscr{R}\left[\left\langle \psi(t) \left| \frac{-i\hbar}{m} \nabla \right| \psi(t) \right\rangle \right] \\
&= \mathscr{R}\left[\frac{-i\hbar}{m} \int_0^{L/N_\mathscr{G}} \mathrm{d}x \; \tilde{\psi}^{(\mu)*}(x;t) \int_0^{L/N_\mathscr{G}} \mathrm{d}x' \right. \\
&\left. \times \left\{ \sum_{\mathscr{R}_{i'},\, \mathscr{R}_i \in \mathscr{G}} \sqrt{\frac{1}{N_\mathscr{G}}} \chi^{\mu*}(\mathscr{R}_{i'}) \bar{K}_{\mathscr{L}}^{N_{\mathrm{der}}=1}(x-x';\Delta t=0) \chi^\mu(\mathscr{R}_i) \sqrt{\frac{1}{N_\mathscr{G}}} \right\} \right. \\
&\left. \times \tilde{\psi}^{(\mu)}(x';t) \right]
\end{aligned}
\tag{54}
$$

We obtained the vibrational properties by computing the Fourier transform of the flux autocorrelation function according to eq 48. The result is presented in Figure 7, and the peaks in the spectra are summarized in Table 5. To resolve the peaks in the spectrum, we compare the peak positions with the energy difference between eigenvalues. As seen in Table 5, the flux autocorrelation function provides results in agreement with eigenvalue calculations. The peaks with high intensities are those that are dipole-allowed. For example, the small bump at around 193 cm^{-1} is identified to be the transition from the first excited state to the second excited state. The peak at around 1302 cm^{-1} corresponds to the transition from the second excited state to the third excited state. The first four eigenstates are shown in Figure 8. The density distribution indicates that the delocalization of the proton is similar to that in a two-dimensional harmonic oscillator. In fact, upon fitting the ground-state wave function to a two-dimensional Gaussian, the energy quanta along the two dimensions are found to be 1488 and 1685 cm^{-1}, which are in close agreement with the $1 \rightarrow 2$ and $1 \rightarrow 3$ transitions in Table 5.

5. CONCLUSIONS

In this study, we have introduced a formalism to treat quantum dynamical effects in extended systems. Specifically, the extended symmetrized distributed approximating functional propagator (ESDAF-P) has been derived for quantum dynamics in extended, condensed-phase systems. In the ESDAF-P approach, the free propagation of a wavepacket is adapted according to the inherent symmetry of the system. The approach is tested for numerical accuracy and efficiency for three cases. We investigated (a) the quantum dynamics of periodic free-particle states, (b) a weakly perturbed, nearly free electron gas problem, and (c) a periodic lattice created from a protonic conductor. In all cases, the formalism is found to be accurate and efficient. Furthermore, for the case of the protonic conductor, we have also demonstrated applicability of ESDAF-P in computing vibrational properties including qunatum nuclear effects arising from the light mass of the hydrogen nucleus as well as from the periodic nature of the problem. This is done by adapting ESDAF-P to the velocity–flux correlation function approach described in ref 4. Future studies will include the simultaneous dynamics of extended quantum dynamical states in conjunction with classical treatment of the remaining nuclei and evolution of electronic structure as is customary in the quantum wavepacket ab initio molecular dynamics (QWAIMD) formalism.

■ APPENDIX A

Benchmarking the Quantum Classical Separation of Electrons and Nuclei in QWAIMD. In ref 4, the QWAIMD formalism has been benchmarked for accuracy in computing vibrational

properties in hydrogen-bonded clusters. Specifically, the ClHCl$^-$ system was treated because it provides significant challenges for accurate modeling of electron–nuclear coupling.[4,119–120] In ref 4, the TDDS implementation of QWAIMD was found to accurately reproduce the experimental spectrum at limited computational cost. The data from ref 4 is excerpted here in Table 6 for convenience. The analysis of trajectories within QWAIMD is facilitated through the introduction of a novel velocity–flux correlation function[4]

$$
C(\omega) = \int_{-\infty}^{+\infty} \mathrm{d}t \; \mathrm{e}^{[-i\omega t]} \{\langle v(t)v(0)\rangle_\mathrm{C} + \langle \mathbf{J}(t)\mathbf{J}(0)\rangle_\mathrm{Q}\}
\tag{A1}
$$

where the wavepacket flux is $\mathbf{J}(t) = \mathscr{R}[\langle\psi(t)|(-i\hbar)/(m)\nabla|\psi(t)\rangle]$. Here, $\mathscr{R}[\cdots]$ represents the real part of the complex number in square parentheses. The symbols $\langle\cdots\rangle_\mathrm{C}$ and $\langle\cdots\rangle_\mathrm{Q}$ represent classical and quantum ensemble averages. We have shown[4] that the expression above describes spectral transition frequencies well for both time-independent and time-dependent Hamiltonians, and this expression is further analyzed in section IVC. Also note that the flux portion of this expression is used in section IVC.

The first block of data in Table 6 depicts harmonic frequencies obtained from electronic structure calculations as well as excitation energies obtained using potential surfaces for the shared proton for frozen Cl–Cl distances. The second block of data is obtained from (a) QWAIMD, (b) NEO-MP2,[119] and (c) CC-VSCF-MP2.[119–122] In the last block, experimental data are provided from velocity modulation spectroscopy[124,125] work in ref 123.

As indicated by the first block of data, the harmonic approximation is inadequate at all levels of electronic structure theory. In fact, borrowing the diatomic molecular spectroscopy notation, the anharmonic constant $w_e x_e$, for ν_3 is a large negative number (see the last column of Table 6) as the spacing between the vibrational levels increases as opposed to that in the harmonic approximation. In Table 6, we also provide corrections to the harmonic approximation by computing three-dimensional proton eigenstate transition energies at the equilibrium Cl–Cl geometries for the respective levels of theory. (See footnote d in Table 6.) Even these calculations only provide an upper bound to the experimental results, though they significantly improve over the harmonic results. Clearly, in addition to anharmonicity, coupling between the proton and chloride motions is critical and is missing in the first block of data provided in Table 6.

The agreement with experiment is drastically improved when QWAIMD is used. The QWAIMD frequencies and band assignments are computed using the velocity–flux correlation function in eq A1 for two different temperatures for each level of theory. These are confirmed by calculating the average $1 \leftarrow 0$ transition energies over the course of a trajectory. As can be seen, the agreement between the QWAIMD results and experiment improves with increasing temperature. Due to a dependence of ν_3 on the simulation temperature, it is important to note that the experiments in ref 123 were performed using velocity modulation spectroscopy where the effective vibrational temperature could be as high as 1000 K.[124,125] Hence, it is not surprising that the higher-temperature QWAIMD results get closer to the experimental result. The high-temperature QWAIMD results for the shared proton stretch (ν_3) in this particular system are in better agreement with experiment as compared to the implementation of correlation-corrected VSCF discussed in ref 119. The reason why QWAIMD exhibits a temperature dependence in its vibrational properties is because as the temperature increases, the Cl–Cl geometry samples larger distances. Because the electronic potential surface adapts to this change within

M

dx.doi.org/10.1021/jp112389m |*J. Phys. Chem. A* XXXX, XXX, 000–000

Table 6. Comparison of QWAIMD with Several Existing Methods for a Highly Anharmonic Cl−H−Cl$^-$ System[a]

level of theory	ν_1 (cm^{-1})	ν_2 (cm^{-1})		ν_3 (cm^{-1})		Cl−Cl dist. (Å)[b]	w_e (cm^{-1})[c]	$w_e x_e$ (cm^{-1})[c]
B3LYP/6-31+G(d,p)	328	834[d]	849[e]	560[d]	949[e]	3.15	827.54	−173.484
B3LYP/aug-cc-PVTZ	324	818[d]	829[e]	582[d]	952[e]	3.15	833.463	−169.508
MP2/6-31+G(d,p)	353	893[d]	907[e]	98[d]	865[e]	3.10	698.037	−217.648
MP2/aug-cc-PVTZ	345	847[d]	863[e]	637[d]	974[e]	3.11	858.043	−181.427
CCSD/aug-cc-PVTZ	181	828[d]	874[e]	833[d]	764[e]	3.14[f]	565.65	−228.137
CCSD(T)/aug-cc-PVTZ	340	842[d]		325[d]		3.12	730.253	−204.83
NEO-MP2(ee+ep)[g]	334	−		−				
CC-VSCF-MP2[h]	327	811		925				
QWAIMD:B3LYP/6-31+G**[i]	300	857		806				
QWAIMD:B3LYP/6-31+G**[j]	254	863		723				
experiment[k]	318	792 ± 9		723				

[a] Data excerpted from ref 4. The first block of data pertains to direct use of electronic structure methods within the harmonic approximation (see text for detail), which is clearly inadmissible for this anhmaronic system. The second block of data provides a comparison of QWAIMD with other well-known techniques that involve either simultaneous electron−nuclear treatment[119] or quantum nuclear effects treated within perturbation theory.[120−122] In the last block, experimental data are provided. [b] The Cl−Cl distance is computed at the optimized geometry obtained at the listed level of electronic structure theory. [c] Potential energy surface harmonic and anharmonic constants. [d] Harmonic frequency corresponding to the optimized geometry. [e] From three-dimensional 1 ← 0 eigenstate transitions. The potential energy surface for the eigenstates is obtained from a full scan of the quantum proton, with the chlorides fixed at optimized geometry positions. Hence, the eigenstates here are corrected for anharmonicity but do not include coupling with the chloride motions. [f] For CCSD, the shared proton is not symmetrically placed along the Cl−Cl axis. This is in contrast with respect to all other optimized geometries here. [g] Reproduced from ref 119. [h] Reproduced from ref 119 based on the implementation of VSCF by Gerber and co-workers.[120−122] [i] On-the-fly electronic structure is performed using B3LYP/6-31+G*; temperature = 323.50 K. [j] On-the-fly electronic structure is performed using B3LYP/6-31+G*; temperature = 714.45 K. [k] Reference 123.
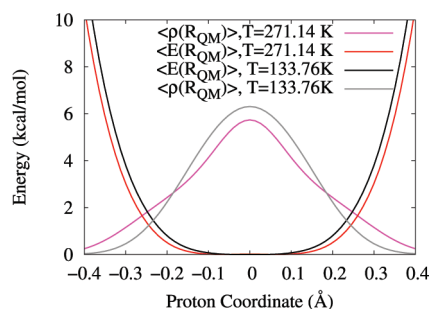

Figure 9. Temperature dependence of vibrational properties in QWAIMD. The system studied is Cl−H−Cl$^-$ as in Table 6.

QWAIMD, this effectively flattens out the potential energy surface on the shared proton along the Cl−Cl distance at larger temperatures. Compare the higher temperature potential depicted using the red curve in Figure 9 with the corresponding lower-temperature black curve. This reduced confinement on the shared proton lowers the transition energies as the wavepackets exhibit a broader distribution at higher temperatures. Compare the gray and magenta wavepacket curves in Figure 9. These lower transition energies for the higher temperature QWAIMD calculation are seen as a red shift in the ν_3 transition computed from the velocity−flux correlation function (eq A1).

■ APPENDIX B

Perturbation Theoretical Treatment of the Weak Potential Problem. The real potential can be written as a sum of a constant term

$$\overline{V} \equiv \frac{1}{Na} \int_0^{Na} V(x) \, dx \tag{B1}$$

and a correction term ΔV that is treated as a perturbation. In the equation above, a is the length of the unit cell, and N is the number of k-points. The solutions to the unperturbed TISE are plane waves e^{ikx}. Utilizing periodic boundary conditions, we have $\phi(x) = \phi(x + Na)$, Thus, the allowed solutions for the unperturbed problem are

$$\phi_k(x) = \frac{1}{\sqrt{Na}} e^{ikx} \qquad k = \frac{2n\pi}{Na}$$
$$n = 0, \pm 1, \pm 2, \; ... \tag{B2}$$

From second-order perturbation theory

$$E_k^{(1)} = \langle k|\Delta V|k \rangle \tag{B3}$$

$$E_k^{(2)} = \sum_{k' \neq k} \frac{|\langle k'|\Delta V|k \rangle|^2}{E_k^{(0)} - E_{k'}^{(0)}} \tag{B4}$$

$$\phi_k^{(1)} = \sum_{k' \neq k} \frac{\langle k'|\Delta V|k \rangle}{E_k^{(0)} - E_{k'}^{(0)}} \phi_{k'}(x) \tag{B5}$$

The kets $|k\rangle'$ and $|k\rangle$ are orthogonal. Hence, $\langle k'|\Delta V|k \rangle = \langle k'|V|k \rangle$ and

$$\langle k'|V|k \rangle = \frac{1}{Na} \int_0^{Na} e^{-i(k' - k)x} V(x) \, dx \tag{B6}$$

Using $V(x + a) = V(x)$ and the change of variable $x = \xi + na$

$$\langle k'|V|k \rangle = \frac{1}{Na} \left\{ \sum_{n=0}^{N-1} e^{-i(k' - k)na} \right\} \int_0^a e^{-i(k'-k)\xi} V(\xi) \, d\xi \tag{B7}$$

N

dx.doi.org/10.1021/jp112389m |J. Phys. Chem. A XXXX, XXX, 000−000

The summation inside of the curly bracket can be classified under two cases

1. If $k' - k = m(2\pi/a)$, m = integers, then $e^{-i(k'-k)na} = 1$; therefore, eq B7 reduces to

$$\langle k'|V|k \rangle = \frac{1}{a}\int_0^a e^{-im(2\pi/a)\xi} V(\xi)\,d\xi \qquad (B8)$$

2. If $k' - k \neq m(2\pi/a)$, the summation reduces to

$$\sum_{n=0}^{N-1} e^{-i(k'-k)na} = \frac{1 - e^{-i(k'-k)Na}}{1 - e^{-i(k'-k)a}} \qquad (B9)$$

Because $k,k' = l(2\pi/Na)$, where l is and integer, $k' - k = (l' - l)(2\pi/Na)$, and the summation in eq B9 is 0. Hence, $\langle k'|V(x)|k \rangle$ is non-zero only when $k' - k = m(2\pi/a)$, and its value is the Fourier coefficient of the potential function. If we substitute the expression for $\langle k'|V|k \rangle$ into eq B5, the expression for the wave function corrected to the first order becomes

$$
\begin{aligned}
\phi_k &= \frac{1}{\sqrt{Na}} e^{ikx} + \sum_{m'=-\infty}^{\infty} \frac{\frac{1}{a}\left[\int_0^a e^{-im'x2\pi/a}V(x)\,dx\right]}{\frac{\hbar^2}{2m}\left[k^2 - \left(k + m'\frac{2\pi}{a}\right)^2\right]} e^{i(k + m'2\pi/a)x} \\
&= \frac{1}{\sqrt{Na}} e^{ikx}\left[1 + \sum_{m'=-\infty}^{\infty} \frac{\frac{1}{a}\left[\int_0^a e^{-im'x2\pi/a}V(x)\,dx\right]}{\frac{\hbar^2}{2m}\left[k^2 - \left(k + m'\frac{2\pi}{a}\right)^2\right]} e^{im'(2\pi/a)x}\right]
\end{aligned}
$$

$$(B10)$$

Equation B10 obeys Bloch symmetry because it is a product of a plane wave and a periodic function.

■ AUTHOR INFORMATION

Corresponding Author
*E-mail: iyengar@indiana.edu.

Present Address
†Current address: Department of Chemistry, Northwestern University, Evanston, IL.

■ ACKNOWLEDGMENT

■ REFERENCES

(1) Iyengar, S. S.; Jakowski, J. J. Chem. Phys. 2005, 122, 114105.
(2) Iyengar, S. S. Theor. Chem. Acc. 2006, 116, 326.
(3) Jakowski, J.; Sumner, I.; Iyengar, S. S. J. Chem. Theory Comput. 2006, 2, 1203–1219.
(4) Sumner, I.; Iyengar, S. S. J. Phys. Chem. A 2007, 111, 10313–10324.
(5) Sumner, I.; Iyengar, S. S. J. Chem. Phys. 2008, 129, 054109.
(6) Li, X.; Iyengar, S. S. J. Chem. Phys. 2010, 132, 184105.
(7) Iyengar, S. S.; Sumner, I.; Jakowski, J. J. Phys. Chem. B 2008, 112, 7601.
(8) Iyengar, S. S. Int. J. Quantum Chem. 2009, 109, 3798.
(9) Hocker, D.; Li, X.; Iyengar, S. S. J. Chem. Theory Comput. 2011, 7, 256.
(10) Pacheco, A. B.; Iyengar, S. S. J. Chem. Phys. 2010, 133, 044105.
(11) Pacheco, A. B.; Iyengar, S. S. J. Chem. Phys. 2011, 134, 074107.
(12) Gerber, R. B.; Buch, V.; Ratner, M. A. J. Chem. Phys. 1982, 77, 3022.
(13) Gerber, R. B.; Ratner, M. A.; Buch, V. Chem. Phys. Lett. 1982, 91, 173.
(14) Buch, V.; Gerber, R. B.; Ratner, M. A. Chem. Phys. Lett. 1983, 101, 44.
(15) Bisseling, R. H.; Kosloff, R.; Gerber, R. B.; Ratner, M. A.; Gibson, L.; Cerjan, C. J. Chem. Phys. 1987, 87, 2760–2765.
(16) Tully, J. C. Faraday Discuss. 1998, 110, 407–419.
(17) Kapral, R.; Ciccotti, G. J. Chem. Phys. 1999, 110, 8919.
(18) Horenko, I.; Salzmann, C.; Schmidt, B.; Schutte, C. J. Chem. Phys. 2002, 117, 11075–11088.
(19) Donoso, A.; Zheng, Y. J.; Martens, C. C. J. Chem. Phys. 2003, 119, 5010.
(20) Brooksby, C.; Prezhdo, O. V. Chem. Phys. Lett. 2001, 346, 463–469.
(21) Prezhdo, O. V.; Brooksby, C. Phys. Rev. Lett. 2000, 86, 3215–3219.
(22) Gindensperger, E.; Meier, C.; Beswick, J. A. J. Chem. Phys. 2000, 113, 9369.
(23) Hammes-Schiffer, S.; Tully, J. C. J. Chem. Phys. 1994, 101, 4657.
(24) Sumner, I.; Iyengar, S. S. J. Chem. Theory Comput. 2010, 6, 1698.
(25) Haile, S. M.; Boysen, D. A.; Chisholm, C. R. I.; Merle, R. B. Nature 2001, 410, 910.
(26) Homouz, D.; Reiter, G.; Eckert, J.; Mayers, J.; Blinc, R. Phys. Rev. Lett. 2007, 98, 115502.
(27) Hudson, B. S.; Verdal, N. Phys. B 2006, 385, 212–215.
(28) Chisholm, C. R. I.; Haile, S. M. Chem. Mater. 2007, 19, 270.
(29) Suzuki, K.; Hayashi, S. Phys. Rev. B 2006, 74, 134303.
(30) Narayanan, S. R.; Yen, S. P.; Liu, L.; Greenbaum, S. G. J. Phys. Chem. B 2006, 110, 3942.
(31) Hayashi, S.; Mizuno, M. Solid State Ionics 2005, 176, 745.
(32) Zhao, X.; Rossi, P.; Barsegov, V.; Zhou, J.; Woodford, J. N.; Harbison, G. S. J. Mol. Struct. 2006, 790, 152–159.
(33) Eckert, J.; Barthes, M.; Klooster, W. T.; Albinati, A.; Aznar, R.; Koetzle, T. F. J. Phys. Chem. B 2001, 105, 19–24.
(34) Reiter, G.; Mayers, J.; Abdul-Redah, T. Phys. B 2006, 385, 234.
(35) Schuster, M. F.; Meyer, W. H. Annu. Rev. Mater. Res. 2003, 33, 233–261.
(36) Kreuer, K. D.; Fuchs, A.; Ise, M.; Spaeth, M.; Maier, J. Electrochim. Acta 1998, 43, 1281–1288.
(37) Iannuzzi, M.; Parrinello, M. Phys. Rev. Lett. 2004, 93, 025901.
(38) Haile, S. M.; Chisholm, C. R. I.; Sasaki, K.; Boysen, D. A.; Uda, T. Faraday Discuss. 2007, 134, 17.
(39) Chuang, S. W.; Hsu, S. L.; Yang, M. L. Eur. Polym. J. 2008, 44, 2202.
(40) Li, Q. F.; Jensen, J. O.; Savinell, R. F.; Bjerrum, N. J. Prog. Polym. Sci. 2009, 34, 449.
(41) Subbaraman, R.; Ghassemi, H.; Zawodzinski, T. Solid State Ionics 2009, 180, 1143.
(42) Knox, C. K.; Voth, G. A. J. Phys. Chem. B 2010, 114, 3205.
(43) Grotthuss, C. J. D. Ann. Chim. 1806, LVIII, 54.
(44) Agmon, N. Chem. Phys. Lett. 1995, 244, 456–462.
(45) Bronstein, L. M.; Karlinsey, R. L.; Yi, Z.; Carini, J.; Werner-Zwanziger, U.; Konarev, P. V.; Svergun, D. I.; Sanchez, A.; Khan, S. Chem. Mater. 2007, 19 (25), 6258–6265.
(46) Nagasubramanian, G.; Bronstein, L.; Carini, J. J. Power Sources 2006, 162, 847.
(47) Persson, K.; Hinuma, Y.; Meng, Y. S.; Van der Ven, A.; Ceder, G. Phys. Rev. B 2010, 82, 125416.
(48) Lee, Y. J.; Lee, Y.; Oh, D.; Chen, T.; Ceder, G.; Belcher, A. M. Nano Lett. 2010, 10, 2433–2440.

O

dx.doi.org/10.1021/jp112389m |J. Phys. Chem. A XXXX, XXX, 000–000

(49) Zhang, M.; Harding, L. B.; Gray, S. K.; Rice, S. A. *J. Phys. Chem. A* **2008**, *112*, 5478–5485.

(50) Trotter, M. F. *Proc. Am. Math. Soc.* **1959**, *10*, 545.

(51) Feit, M. D.; Fleck, J. A. *J. Chem. Phys.* **1982**, *78*, 301.

(52) Nelson, E. *J. Math. Phys.* **1964**, *5*, 332.

(53) Feit, M. D.; Fleck, J. A. *J. Chem. Phys.* **1983**, *79*, 301.

(54) Feit, M. D.; Fleck, J. A. *J. Chem. Phys.* **1984**, *80*, 2578.

(55) DeVries, P. In *Atomic and molecular processes with short intense laserpulses*; NATO ASI Series B; Physics; Bandrauk, A. D., Ed.; Plenum Press: New York, 1988; Vol. 171, p 481.

(56) Kosloff, D.; Kosloff, R. *J. Comput. Phys.* **1983**, *52*, 35.

(57) Kosloff, D.; Kosloff, R. *J. Chem. Phys.* **1983**, *79*, 1823.

(58) Iyengar, S. S.; Kouri, D. J.; Hoffman, D. K. *Theor. Chem. Acc.* **2000**, *104*, 471.

(59) Leforestier, C.; Bisseling, R. H.; Cerjan, C.; Feit, M. D.; Freisner, R.; Guldberg, A.; Hammerich, A.; Jolicard, D.; Karrlein, W.; Meyer, H. D.; Lipkin, N.; Roncero, O.; Kosloff, R. *J. Comput. Phys.* **1991**, *94*, 59.

(60) Tal-Ezer, H.; Kosloff, R. *J. Chem. Phys.* **1984**, *81*, 3967.

(61) Kosloff, R. *Annu. Rev. Phys. Chem.* **1994**, *45*, 145.

(62) Hartke, B.; Kosloff, R.; Ruhman, S. *Chem. Phys. Lett.* **1986**, *158*, 223.

(63) Neuhauser, D. *J. Chem. Phys.* **1991**, *95*, 4927.

(64) Huang, Y.; Iyengar, S. S.; Kouri, D. J.; Hoffman, D. K. *J. Chem. Phys.* **1996**, *105*, 927.

(65) Gray, S. K.; Balint-Kurti, G. G. *J. Chem. Phys.* **1998**, *226*, 950.

(66) Arfken, G. *Mathematical Methods for Physicists*; Academic Press: New York, 1985.

(67) Mowrey, R. C.; Kouri, D. J. *J. Chem. Phys.* **1986**, *84*, 6466.

(68) Feynman, R. P.; Hibbs, A. R. *Quantum Mechanics and Path Integrals*; McGraw-Hill Book Company: New York, 1965.

(69) Schulman, L. S. *Techniques and Applications of Path Integration*; John Wiley and Sons, Inc.: New York, 1986.

(70) Chandler, D.; Wolynes, P. G. *J. Chem. Phys.* **1981**, *74*, 4078.

(71) Miller, W. H.; Schwartz, S. D.; Tromp, J. W. *J. Chem. Phys.* **1983**, *79*, 4889.

(72) Berne, B. J.; Thirumalai, D. *Annu. Rev. Phys. Chem.* **1986**, *37*, 401–424.

(73) Makri, N. *Comput. Phys. Commun.* **1991**, *63*, 389–414.

(74) Cao, J.; Voth, G. A. *J. Chem. Phys.* **1994**, *100*, 5093.

(75) Cao, J.; Voth, G. A. *J. Chem. Phys.* **1994**, *100*, 5106.

(76) Wyatt, R. E., Zhang, J. Z. H., Eds. *Dynamics of Molecules and Chemical Reactions*; Marcel Dekker Inc.: New York, 1996.

(77) Deumens, E.; Diz, A.; Longo, R.; Öhrn, Y. *Rev. Mod. Phys.* **1994**, *66*, 917.

(78) Lill, J. V.; Parker, G. A.; Light, J. C. *Chem. Phys. Lett.* **1982**, *89*, 483.

(79) Light, J. C.; Hamilton, I. P.; Lill, J. V. *J. Chem. Phys.* **1985**, *82*, 1400.

(80) Colbert, D. T.; Miller, W. H. *J. Chem. Phys.* **1992**, *96*, 1982–1991.

(81) Hoffman, D. K.; Nayar, N.; Sharafeddin, O. A.; Kouri, D. J. *J. Phys. Chem.* **1991**, *95*, 8299.

(82) Hoffman, D. K.; Kouri, D. J. *J. Phys. Chem.* **1992**, *96*, 9631.

(83) Hoffman, D. K.; Arnold, M.; Kouri, D. J. *J. Phys. Chem.* **1992**, *96*, 6539–6545.

(84) Hoffman, D. K.; Marchioro, T. L.; Arnold, M.; Huang, Y. H.; Zhu, W.; Kouri, D. J. *J. Math. Chem.* **1996**, *20*, 117–140.

(85) Hoffman, D. K.; Wei, G. W.; Zhang, D. S.; Kouri, D. J. *Phys. Rev. E* **1998**, *57*, 6152–6160.

(86) Hoffman, D. K.; Wei, G. W.; Kouri, D. J. *J. Math. Chem.* **1999**, *25*, 235–244.

(87) Huang, Y.; Kouri, D. J.; Arnold, M.; Thomas L. Marchioro, I.; Hoffman, D. K. *Comput. Phys. Commun.* **1994**, *80*, 1.

(88) Kouri, D. J.; Huang, Y.; Hoffman, D. K. *Phys. Rev. Lett.* **1995**, *75*, 49–52.

(89) Wei, G. W.; Althorpe, S. C.; Kouri, D. J.; Hoffman, D. K. *J. Chem. Phys.* **1998**, *108*, 7065.

(90) Wei, G. W.; Althorpe, S. C.; Zhang, D. S.; Kouri, D. J.; Hoffman, D. K. *Phys. Rev. A* **1998**, *57*, 3309.

(91) Iyengar, S. S.; Parker, G. A.; Kouri, D. J.; Hoffman, D. K. *J. Chem. Phys.* **1999**, *110*, 10283–10298.

(92) Chandler, C.; Gibson, A. *J. Approx. Theory* **1999**, *100*, 233.

(93) Hoffman, D. K.; Gunaratne, G. H.; Zhang, D. S.; Kouri, D. J. *Chaos* **2000**, *10*, 240.

(94) Hu, S.; Goldman, D. I.; Kouri, D. J.; Hoffman, D. K.; Swinney, H. L.; Gunaratne, G. H. *Nonlinearity* **2004**, *17* (4), 1535.

(95) Shen, L. X.; Papadakis, M.; Kakadiaris, I. A.; Konstantinidis, I.; Kouri, D. J.; Hoffman, D. K. *IEEE Trans. Image Process.* **2006**, *15*, 1254.

(96) Schlegel, H. B.; Millam, J. M.; Iyengar, S. S.; Voth, G. A.; Daniels, A. D.; Scuseria, G. E.; Frisch, M. J. *J. Chem. Phys.* **2001**, *114*, 9758.

(97) Iyengar, S. S.; Schlegel, H. B.; Voth, G. A.; Millam, J. M.; Scuseria, G. E.; Frisch, M. J. *Isr. J. Chem.* **2002**, *42*, 191–202.

(98) Shannon, C. *Bell Syst. Tech. J.* **1948**, *27*, 279–423.

(99) Shannon, C. *Proc. IEEE* **1998**, *86*, 447.

(100) Wehrl, A. *Rev. Mod. Phys.* **1978**, *50*, 221.

(101) Wehner, S.; Winter, A. *J. Math. Phys.* **2008**, *49*, 062105.

(102) Bartels, R. H.; Beatty, J. C.; Barsky, B. A. *An Introduction to Splines for use in computergraphics and geometric modeling*; Morgan Kaufman Publishers, Inc.: Los Altos, CA, 1987.

(103) Li, X.; Oomens, J.; Eyler, J. R.; Moore, D. T.; Iyengar, S. S. *J. Chem. Phys.* **2010**, *132*, 244301.

(104) Kudin, K. N.; Scuseria, G. E. *Phys. Rev. B* **2000**, *61*, 16440.

(105) Tinkham, M. *Group theory and quantum mechanics*; McGraw-Hill Book Company: New York, 1964.

(106) Iyengar, S. S.; Kouri, D. J.; Parker, G. A.; Hoffman, D. K. *Theor. Chem. Acc.* **2000**, No. 103, 507–517.

(107) Li, X.; Tully, J. C.; Schlegel, H. B.; Frisch, M. J. *J. Chem. Phys.* **2005**, *123* (8), 084106.

(108) Micha, D. A. *J. Phys. Chem. A* **1999**, *103*, 7562–7574.

(109) Agmon, N. *J. Phys. Chem. A* **1998**, *102*, 192.

(110) Yu, S.; Zhao, S.; Wei, G. W. *J. Comput. Phys.* **2005**, *206*, 727–780.

(111) Sorensen, D. C. *SIAM J. Mater. Anal. App.* **1992**, *13*, 357–385.

(112) Golub, G. H.; van Loan, C. F. *Matrix Computations*; The Johns Hopkins University Press: Baltimore, MD, 1996.

(113) Parlett, B. N.; Saad, Y. *Linear Algebra and its Applications* **1987**, *88/89*, 575–595.

(114) Drude, P. *Ann. Phys.* **1900**, *1*, 578.

(115) Kittel, C. *Introduction to Solid State Physics*; John Wiley & Sons, Inc.: New York, Chichester, Brisbane, Toronto, Singapore, 1996.

(116) Dunlap, B. I. *J. Chem. Phys.* **1983**, *78*, 3140.

(117) Dunlap, B. I. *J. Mol. Struct.: THEOCHEM* **2000**, *529*, 37.

(118) Press, W. H.; Teukolsky, S. A.; Vetterling, W. T.; Flannery, B. P. *Numerical Recipes in C*; Cambridge University Press: New York, 1992.

(119) Swalina, C.; Hammes-Schiffer, S. *J. Phys. Chem. A* **2005**, *109*, 10410.

(120) Gerber, R. B.; Ratner, M. A. *J. Chem. Phys.* **1988**, *70*, 97–132.

(121) Matsunaga, N.; Chaban, G. M.; Gerber, R. B. *J. Chem. Phys.* **2002**, *117*, 3541.

(122) Jung, J. O.; Gerber, R. B. *J. Chem. Phys.* **1996**, *105*, 10332.

(123) Kawaguchi, K. *J. Chem. Phys.* **1988**, *88*, 4186–4189.

(124) Gudeman, C.; Begemann, M.; Pfaff, J.; Saykally., R. *J. Phys. Rev. Lett.* **1983**, *50*, 727.

(125) Saykally, R. *Science* **1988**, *239*, 157.